



UNIVERSITY OF LEEDS

This is a repository copy of *Small-scale lithospheric heterogeneity characterization using Bayesian inference and energy flux models*.

White Rose Research Online URL for this paper:  
<https://eprints.whiterose.ac.uk/176346/>

Version: Accepted Version

---

**Article:**

González Álvarez, I, Rost, S, Nowacki, A [orcid.org/0000-0001-7669-7383](https://orcid.org/0000-0001-7669-7383) et al. (1 more author) (Accepted: 2021) Small-scale lithospheric heterogeneity characterization using Bayesian inference and energy flux models. *Geophysical Journal International*. ISSN 0956-540X (In Press)

---

This item is protected by copyright. This is an author produced version of an article, accepted for publication in *Geophysical Journal International*. Uploaded in accordance with the publisher's self-archiving policy.

**Reuse**

Items deposited in White Rose Research Online are protected by copyright, with all rights reserved unless indicated otherwise. They may be downloaded and/or printed for private study, or other acts as permitted by national copyright laws. The publisher or other rights holders may allow further reproduction and re-use of the full text version. This is indicated by the licence information on the White Rose Research Online record for the item.

**Takedown**

If you consider content in White Rose Research Online to be in breach of UK law, please notify us by emailing [eprints@whiterose.ac.uk](mailto:eprints@whiterose.ac.uk) including the URL of the record and the reason for the withdrawal request.



[eprints@whiterose.ac.uk](mailto:eprints@whiterose.ac.uk)  
<https://eprints.whiterose.ac.uk/>

# Small-scale lithospheric heterogeneity characterization using Bayesian inference and energy flux models

Itahisa González Álvarez<sup>1</sup>, Sebastian Rost<sup>1</sup>, Andy Nowacki<sup>1</sup>,  
and Neil D. Selby<sup>2</sup>

<sup>1</sup>School of Earth and Environment, University of Leeds, LS2 9JT, UK. E-mail: eeinga@leeds.ac.uk  
<sup>2</sup>AWE Blacknest, Brimpton, Reading, RG7 4RS, UK

## SUMMARY

Observations from different disciplines have shown that our planet is highly heterogeneous at multiple scale lengths. Still, many seismological Earth models tend not to include any small-scale heterogeneity or lateral velocity variations, which can affect measurements and predictions based on these homogeneous models. In this study, we describe the lithospheric small-scale isotropic heterogeneity structure in terms of the intrinsic, diffusion and scattering quality factors, as well as an autocorrelation function, associated with a characteristic scale length ( $a$ ) and root mean square (RMS) fractional velocity fluctuations ( $\epsilon$ ). To obtain this characterization, we combined a single-layer and a multi-layer energy flux models with a new Bayesian inference algorithm. Our synthetic tests show that this technique can successfully retrieve the input parameter values for 1- or 2-layer models and that our Bayesian algorithm can resolve whether the data can be fitted by a single set of parameters or a range of models is required instead, even for very complex posterior probability distributions. We applied this technique to three seismic arrays in Australia: Alice Springs array (ASAR), Warramunga Array (WRA) and Pilbara Seismic Array (PSAR). Our single-layer model results suggest intrinsic and diffusion attenuation are strongest for ASAR, while scattering and total attenuation are similarly strong for ASAR and WRA. All quality factors take higher values for PSAR than for the other two arrays, implying that the structure beneath this array is less attenuating and heterogeneous than for ASAR or WRA. The multi-layer model results show

the crust is more heterogeneous than the lithospheric mantle for all arrays. Crustal correlation lengths and RMS velocity fluctuations for these arrays range from  $\sim 0.2 - 1.5$  km and  $\sim 2.3 - 3.9$  % respectively. Parameter values for the upper mantle are not unique, with combinations of low values of the parameters ( $a < 2$  km and  $\epsilon < \sim 2.5$  %) being as likely as those with high correlation length and velocity variations ( $a > 5$  km and  $\epsilon > \sim 2.5$  % respectively). We attribute the similarities in the attenuation and heterogeneity structure beneath ASAR and WRA to their location on the proterozoic North Australian Craton, as opposed to PSAR, which lies on the archaean West Australian Craton. Differences in the small-scale structure beneath ASAR and WRA can be ascribed to the different tectonic histories of these two regions of the same craton. Overall, our results highlight the suitability of the combination of an energy flux model and a Bayesian inference algorithm for future scattering and small-scale heterogeneity studies, since our approach allows us to obtain and compare the different quality factors, while also giving us detailed information about the trade-offs and uncertainties in the determination of the scattering parameters.

**Keywords:** Structure of the Earth, Australia, statistical methods, coda waves, seismic attenuation, wave scattering and diffraction.

# 1 INTRODUCTION

2 The Earth is heterogeneous on a variety of scales, ranging from the grain scale  
3 to scales of hundreds of kilometers. This heterogeneity is evident in data from  
4 geo-disciplines with varying sensitivity to different scales, such as geochemistry,  
5 mineralogy or seismology (e.g. Wu and Aki, 1988). Due to the seismic wave-  
6 lengths, most seismological Earth models are laterally homogeneous or smoothly  
7 varying, with a lack of small-scale heterogeneity (e.g. Helmberger, 1968; Dziewon-  
8 ski and Anderson, 1981; Kennett and Engdahl, 1991; Randall, 1994). This limits  
9 our understanding of high-frequency seismic wave propagation and challenges in  
10 seismic imaging of small-scale heterogeneities remain.

11 Many seismic studies published before the 1970s were based on laterally ho-  
12 mogeneous Earth models (e.g. Alexander and Phinney, 1966) which were able  
13 to explain the propagation of long period signals, but failed to explain high fre-  
14 quency seismograms. Aki (1969) showed that the power spectra of coda waves for  
15 a given station are independent of epicentral distance and earthquake magnitude.  
16 He proposed that codas were caused by backscattered energy from discrete het-  
17 erogeneities randomly distributed beneath the stations. The presence and shape  
18 of the coda strongly depends on the heterogeneity structure and, therefore, the  
19 geology beneath the station. Later studies (e.g. Aki and Chouet, 1975; Rautian  
20 and Khalturin, 1978) showed that the stable decay in coda wave amplitude was  
21 also independent of epicentral distance and source mechanism, fully supporting  
22 the scattering hypothesis.

23 Methods to study heterogeneity and scattering within the Earth vary depend-  
24 ing on the type of the heterogeneity. Many seismological studies use deterministic  
25 methods to characterize the structure of the Earth (e.g. Christensen and Mooney,  
26 1995; Zelt and Barton, 1998) or to find individual scatterers and try to obtain their

27 particular characteristics and locations (e.g. Etgen et al., 2009). Marchenko imag-  
28 ing (e.g. Thorbecke et al., 2017; van der Neut et al., 2015) or migration techniques  
29 (e.g. Etgen et al., 2009) are often used in reflection seismology to study shallow  
30 structure and are a good example of deterministic methods. These techniques  
31 tend to have limited spatial resolution due to the wavelength of the studied waves  
32 and do not always take into account small-scale heterogeneities (on the order of  
33 magnitude of the wavelength or smaller), therefore failing to explain or reproduce  
34 the complex coda waves we see in seismograms. A different approach that par-  
35 tially overcomes these issues uses a stochastic description of the heterogeneity (e.g.  
36 Korn, 1990, 1997; Margerin, 2005; Hock et al., 2004; Ritter et al., 1998). This ap-  
37 proach (e.g. Frankel and Wennerberg, 1987; Shapiro and Kneib, 1993; Hock et al.,  
38 2004; Sato and Emoto, 2018) provides a statistical description of the structure and  
39 determines the integrated effect of heterogeneity on propagating seismic waves, so  
40 the characteristics and locations of individual scatterers are not relevant. Studies  
41 show the crust and lithospheric heterogeneity to be statistically complex and the  
42 necessity of heterogeneous Earth models that are capable of explaining not only  
43 the main waveforms but also coda waves (e.g. Aki, 1973; Flatté and Wu, 1988;  
44 Langston, 1989).

45 Several methods allow us to study the propagation of seismic waves through  
46 heterogeneous stochastic media and characterise the scattering and attenuation  
47 properties of the Earth. Single-scattering perturbation theory (e.g. Aki and Chouet,  
48 1975; Sato, 1977, 1984) was one of the first methods designed for this purpose. It  
49 considers scattering to be a weak process and coda waves the superposition of  
50 single scattered waves generated at randomly distributed heterogeneities within  
51 the Earth. It often makes use of the Born approximation (e.g. Sato et al., 2012),  
52 a first-order perturbation condition which does not take into account the energy

53 loss from the primary waves. As a result, energy is not conserved in the scattering  
54 process (e.g. Aki and Chouet, 1975). Sato (2006), Sato (2007) and Emoto et al.  
55 (2010) later set the basis for future synthesis of vector wave envelopes studies by  
56 extending the Markov approximation for scalar waves and developing a series of  
57 algorithms to synthesize vector wave envelopes in 3-D Gaussian random elastic  
58 media. Recently, many studies have used Radiative Transfer Theory (RTT), a  
59 technique initially developed for light propagation (Chandrasekhar, 1950) which  
60 has been significantly improved and expanded (e.g. Margerin et al., 1998; Przybilla  
61 and Korn, 2008; Nakahara and Yoshimoto, 2011; Sanborn et al., 2017; Sato and  
62 Emoto, 2017, 2018; Hirose et al., 2019; Margerin et al., 2019) since its first appli-  
63 cations to seismology (e.g. Wu, 1985; Gusev and Abubakirov, 1987). In particular,  
64 the development and improvement of Monte Carlo simulations and analytical ap-  
65 proaches to solve the radiative transfer equations have made it possible to apply  
66 RTT to a wide variety of tectonic and geological settings (e.g. Gaebler et al.,  
67 2015b,a; Fielitz and Wegler, 2015; Margerin and Nolet, 2003; Hirose et al., 2019).  
68 Other methods to analyse coda energy and study lithospheric heterogeneity have  
69 been proposed and are also widely used (e.g. coda normalization method (Aki,  
70 1980), multiple lapse time window analysis (e.g. Fehler et al., 1992), coda wave  
71 interferometry (e.g. Snieder, 2006), etc). While these methods are able to charac-  
72 terize the heterogeneity structure of the Earth, they all use approximations or are  
73 computationally expensive.

74 In this study, we combine two stochastic methods, the single layer modified  
75 Energy Flux Model (EFM, Korn, 1990) and the depth dependent Energy Flux  
76 Model (EFMD, Korn, 1997), with a Bayesian inversion algorithm which allows us  
77 to characterise small-scale lithospheric heterogeneity by fully exploring the scatter-  
78 ing parameter space and obtain information about the trade offs and uncertainties

79 in the determination of the parameters. We applied these methods to a large  
80 dataset of teleseismic events recorded at three seismic arrays of the Australian Na-  
81 tional Seismic Network: Pilbara Seismic Array (PSAR), and Alice Springs Array  
82 (ASAR) and Warramunga Array (WRA), which are also primary seismic arrays  
83 from the International Monitoring System (IMS) network, the worldwide network  
84 built to ensure compliance with the Comprehensive Test Ban Treaty (CTBT).

## 85 **2 METHODS**

86 We use the random medium approach, which considers the propagation of seis-  
87 mic waves through a medium with constant background velocity and density and  
88 random heterogeneities distributed according to a given autocorrelation function  
89 (ACF) and linearly related through Birch's law (Birch, 1961). The ACF depends  
90 on the RMS fractional velocity fluctuations,  $\epsilon$ , and the characteristic or correlation  
91 length,  $a$ , which defines the spatial variation of the heterogeneities. By obtaining  
92 these parameters, it is possible to obtain a statistical description of the sampled  
93 structure that reveals the strength of the scattering experienced by seismic waves.  
94 The modified Energy Flux Model (EFM) and depth-dependent Energy Flux Model  
95 (EFMD) can be used for both weak and strong scattering (e.g. Korn, 1990; Hock  
96 and Korn, 2000; Hock et al., 2004) and allow determining the best-fitting ACF of  
97 the heterogeneous medium. Both methods work under the assumption of planar  
98 wavefronts and vertical or near-vertical incidence from below on a single scattering  
99 layer (EFM) or stack of layers (EFMD), conditions well met by teleseismic events,  
100 allowing the study of the heterogeneity structure in seismically quiet regions.

101 Here we present a short introduction to the EFM and EFMD. Full details  
102 about the methods can be found in Korn (1990), Korn (1997), Hock and Korn  
103 (2000) and Hock et al. (2004).

### 104 **2.1 The Modified Energy Flux Model for a single scat-** 105 **tering layer**

106 When a plane wavefront enters a heterogeneous unlayered medium from below,  
107 part of the energy propagates with the ballistic wavefront, while part forms the  
108 forward scattered coda energy that arrives later at the surface and some energy



109 scatters back into the half-space. Total energy  $E_{tot}$  is conserved in this process  
 110 and we can write it in terms of frequency,  $\omega$ , and time,  $t$ , as

$$E_{tot}(\omega, t) = E_d(\omega, t) + E_c(\omega, t) + E_{diff}(\omega, t), \quad (1)$$

111 with  $E_d$  being the energy of the direct wave,  $E_c$  the energy transferred from  
 112 the direct wave into the coda (forward scattered) and  $E_{diff}$  the energy diffusion  
 113 (backscattering) from the current layer back into the half-space. The energy that is  
 114 transferred from the incoming wavefront to the scattered coda and the backscat-  
 115 tering to the half-space can be expressed as an energy loss for the direct wave,  
 116 controlled by a quality factor  $Q_s$  for scattering and  $Q_{diff}$  for diffusion. To take  
 117 into account anelastic (intrinsic) attenuation, we use the quality factor  $Q_i$ . The  
 118 EFM assumes spatially homogeneous coda energy within the scattering layer. En-  
 119 ergy transfer into the coda due to scattering or anelastic losses stops once the  
 120 ballistic wave leaves the scattering layer after totally reflecting at the free surface,  
 121 while diffusion out of the scattering layer can continue after that.

122 A linear least-squares fit of the theoretical coda power spectral density allows  
 123 us to calculate the coda decay rate,  $a_1$ , and its amplitude at zero time,  $a_0$  (Korn,  
 124 1990, 1993). The values of  $Q_i$  and  $Q_{diff}$  at 1 Hz,  $Q_{i0}$  and  $Q_{d0}$ , can be obtained  
 125 from values of  $a_1$  at different frequencies via

$$a_1(\omega) = -2\pi[Q_{d0}^{-1} + Q_{i0}^{-1}(\omega/2\pi)^{1-\alpha}] \log_{10} e, \quad (2)$$

126 where  $\alpha$  is the exponent controlling the frequency dependence of  $Q_i$  (Korn, 1990).  
 127 To determine  $Q_{diff}$  and  $Q_i$  at different frequency bands, we then use:

$$Q_{diff}(\omega) = Q_{d0}\omega/2\pi \quad (3)$$

$$Q_i(\omega) = Q_{i0}(\omega/2\pi)^\alpha \quad (4)$$

128 Laboratory measurements of  $\alpha$  have shown that it probably remains below  
 129 1 for most of the frequency range considered here (Korn, 1990, and references  
 130 therein). Our attempts at obtaining  $\alpha$  as a third free parameter in the least-  
 131 squares inversion of Eq. 2 revealed a very complicated trade-off with  $Q_{i0}$  and  
 132  $Q_{d0}$ , with high values of  $\alpha$  corresponding to negative values of  $Q_{i0}$  and/or  $Q_{d0}$ .  
 133 Therefore, we limited  $\alpha$  to the range of 0.0 - 0.6, in steps of 0.1, and chose the  
 134 value that minimised the misfit to the data. The impossibility to fully invert for  $\alpha$   
 135 makes it difficult to accurately calculate  $Q_i$  within the EFM, but has a minor effect  
 136 in the determination of  $Q_{diff}$  (Korn, 1990). For our range of source distances,  $Q_i$   
 137 is generally much larger than  $Q_{diff}$  (Korn, 1990), which reduces the impact of this  
 138 limitation of the EFM inversion.

139 The coda amplitude at zero time,  $a_0$ , is related to  $Q_s$  through

$$Q_s \approx 2I_D\omega^{1-a_0}, \quad (5)$$

140  $I_D$  being the integral of the squared amplitude envelope,  $A^2(t; \omega)$ , over the time  
 141 window of the direct wave arrival (Hock and Korn, 2000). We can then use the  
 142 relationships between  $Q_s^{-1}$  and the structural parameters for different types of  
 143 ACFs obtained by Fang and Müller (1996) to determine the type of ACF that fits  
 144 the data best, as well as a first estimation of the correlation length ( $a$ ) and the RMS  
 145 velocity fluctuations ( $\epsilon$ ) for a single scattering layer. The eight one octave-wide  
 146 frequency bands we used in our analysis for both methods are shown in Table 1.  
 147 Given the similarity between different ACFs within our frequency range of interest,  
 148 and despite the possibility to determine the type of ACF of the scattering structure  
 149 using the EFM, we decided to assume an exponential ACF for this study, since

**Table 1:** List of all frequency bands used in this study.

Frequency band	A	B	C	D	E	F	G	H
Minimum frequency (Hz)	0.5	0.75	1	1.5	2	2.5	3	3.5
Maximum frequency (Hz)	1.0	1.5	2	3	4	5	6	7

150 previous studies have proposed it as an appropriate ACF for teleseismic scattering  
 151 studies (Shearer and Earle, 2004).

152 Finally, we calculated the combined quality factor,  $Q_{comb}$ , as the combination  
 153 of all three quality factors:

$$\frac{1}{Q_{comb}} = \frac{1}{Q_{diff}} + \frac{1}{Q_i} + \frac{1}{Q_s} \tag{6}$$

154 Please note that  $Q_{comb}$ , as opposed to other quality factors, is not related  
 155 to the energy decay of the wavefield nor it is applied to any specific part of the  
 156 seismogram. Its only intent is to summarise the total coda attenuation and make  
 157 it easier to compare our results from the different arrays.

## 158 **2.2 The Energy Flux Model for depth-dependent het-** 159 **erogeneity**

160 Korn (1997) modified the EFM to include depth-dependent heterogeneity. In this  
 161 model, a plane wavefront enters a stack of  $N$  heterogeneous layers from below.  
 162 Each layer  $j$  has its own characteristic transit time  $\delta t_j$  and scattering quality  
 163 factor  $Q_{s_j}$ , which is calculated from the structural parameters  $a_j$  and  $\epsilon_j$  (Fig. 1)  
 164 using the analytical approximation for isotropic exponential media obtained by  
 165 Fang and Müller (1996). The stack of layers is symmetric with respect to the  
 166 free surface, which is located at the center of the stack to take into account the  
 167 reflection of the wavefront.

168 For a given angular frequency  $\omega_c$ , the normalised coda energy envelope of a  
 169 velocity seismogram at the free surface is computed from the squared amplitude  
 170 envelope  $A^2(t; \omega_c)$  and is related to the energy balance within the different layers  
 171 in the model through

$$\sqrt{\frac{A^2(t; \omega_c)}{I_D}} = \sqrt{\frac{2E_{C_N}(t; \omega_c)}{t_N E_D(t_N; \omega_c)}}, \quad (7)$$

172 with  $E_{C_N}(t; \omega_c)$  being the spectral coda energy density of the layer containing the  
 173 free surface,  $t_N$  the traveltime from the bottom of the stack of layers to the free  
 174 surface and  $E_D(t; \omega_c)$  the energy density of the direct wave at the free surface.  $Q_s$   
 175 and  $Q_i$  control the decay of the direct wave energy over time due to scattering and  
 176 intrinsic attenuation via

$$E_D(t_j; \omega) = E_D(t_{j-1}; \omega_c) e^{-\omega(t_j - t_{j-1})(Q_{s_j}^{-1} + Q_{i_j}^{-1})}, \quad (8)$$

177 where  $t_j$  represents the one-way travel time through each layer. The energy balance  
 178 within layer  $j$  ( $j = 1, \dots, N$ ) is represented by

$$\begin{aligned} \frac{dE_{C_j}}{dt} = & -\frac{1}{4\delta t_j} E_{C_j}(t) H(t - t_j) \\ & -\frac{1}{4\delta t_j} E_{C_j}(t) H(t - t_{j-1}) \\ & +\frac{1}{4\delta t_{j-1}} E_{C_{j-1}}(t) H(t - t_{j-1}) \\ & +\frac{1}{4\delta t_{j+1}} E_{C_{j+1}}(t) H(t - t_j) \\ & -\frac{\omega}{Q_{i_j}} E_{C_j}(t) H(t - t_{j-1}) \\ & +\frac{\omega}{Q_{s_j}} E_D(t) H(t - t_{j-1}) H(t_j - t) \end{aligned}, \quad (9)$$

179 where  $H$  is the Heaviside function. The first two terms of Eq. 9 describe the energy

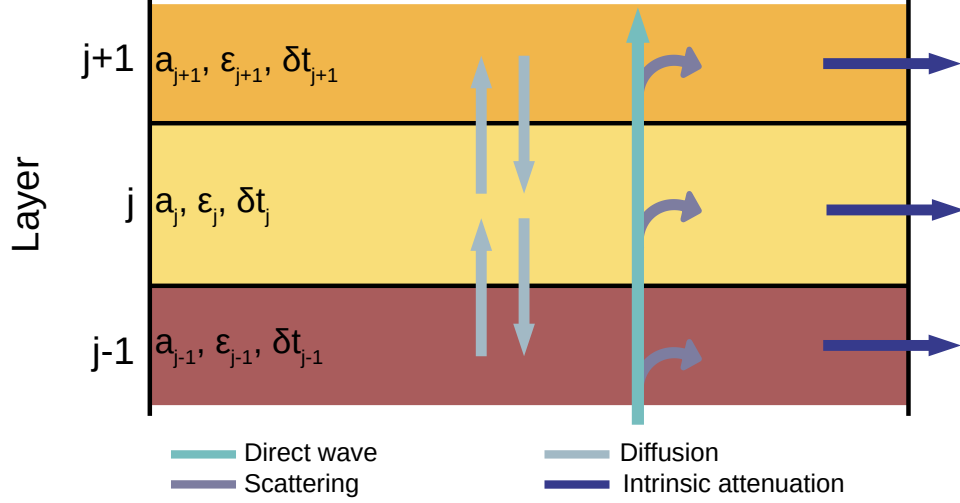


Figure 1: Total energy balance for layer  $j$ , according to the EFMD. (After Korn, 1997).

180 flux from layer  $j$  to the layers above and below, while the next two terms describe  
 181 the opposite flux from the neighbouring layers into layer  $j$ . The last two terms  
 182 represent the anelastic or intrinsic energy loss and the direct wave energy input  
 183 into the layer. In practice, for a given model  $\mathbf{m}$ , comprising a single value of  $a$  and  
 184  $\epsilon$  for each layer in the stack,  $E_D$  is calculated for each time sample using Eq. 8,  
 185 starting from the measured energy value at the free surface. Then, the system of  
 186 linear differential equations in Eq. 9 is solved for each layer in the model. Finally,  
 187 synthetic coda envelopes are calculated for each frequency band using Eq. 7.

### 188 2.2.1 Bayesian inference

189 We use a Bayesian approach to obtain the values of the structural parameters for  
 190 each layer in the model (e.g. Tarantola, 2005). In this approach, the aim is not to  
 191 obtain a best fitting model, but to test a large number of models with parameters  
 192 drawn from a prior probability distribution  $p(\mathbf{m})$  (or prior) defined by our previous

193 knowledge on them. In our case, we assume we have no previous knowledge on  
 194 the value of the parameters and use a uniform prior.

195 The likelihood associated with model  $\mathbf{m}$ ,  $p(\mathbf{d}|\mathbf{m})$ , is the probability of observing  
 196 our data,  $\mathbf{d}$ , given the model parameters in  $\mathbf{m}$ . We used the Mahalanobis distance  
 197  $\Phi(\mathbf{m})$  (Mahalanobis, 1936) between  $\mathbf{d}$ , with variance-covariance matrix  $\mathbf{C}$ , and the  
 198 synthetic envelopes  $g(\mathbf{m})$ , to calculate the fit to our data:

$$\Phi(\mathbf{m}) = (g(\mathbf{m}) - \mathbf{d})^T \mathbf{C}^{-1} (g(\mathbf{m}) - \mathbf{d}), \quad (10)$$

199 which we then applied to the calculation of the likelihood of model  $\mathbf{m}$ :

$$p(\mathbf{d}|\mathbf{m}) = \frac{1}{\sqrt{(2\pi)^n |\mathbf{C}|}} \exp\left(\frac{-\Phi(\mathbf{m})}{2}\right) \quad (11)$$

200 Bayes' theorem (Bayes, 1763) allows us to calculate the corresponding sample of  
 201 the posterior probability distribution (or posterior), that is, the probability density  
 202 associated with model  $\mathbf{m}$ , or  $p(\mathbf{m}|\mathbf{d})$ :

$$p(\mathbf{m}|\mathbf{d}) \propto p(\mathbf{d}|\mathbf{m})p(\mathbf{m}) \quad (12)$$

203 We create an initial model by selecting a random value for the correlation length  
 204 and velocity fluctuations in all layers in the  $(a_{min}, a_{max})$  or  $(\epsilon_{min}, \epsilon_{max})$  intervals,  
 205 with  $a_{min} = 0.2\lambda_{min}$  [m],  $a_{max} = 2\lambda_{max}$  [m] ( $\lambda_{min}$  and  $\lambda_{max}$  being the mini-  
 206 mum and maximum wavelengths in the layer, depending on signal frequency and  
 207 background velocity),  $\epsilon_{min} = 4.5 \cdot 10^{-3}$  % and  $\epsilon_{max} = 10$  %. These maximum  
 208 and minimum values were chosen considering the relevant range for detectable  
 209 scattering while being geologically feasible (e.g Korn, 1993; Hock et al., 2004).

210 We then applied the Metropolis-Hastings algorithm (Metropolis and Ulam,

211 1949; Metropolis et al., 1953; Hastings, 1970) to sample the posterior probability  
 212 distribution and generate our ensemble of solution models. This way, at every  
 213 time step, this Markov Chain Monte Carlo (MCMC) algorithm generates a new  
 214 model  $\mathbf{m}'$  by randomly choosing one of the parameters in the previous model ( $\mathbf{m}$ )  
 215 and updating its value by adding a random number in the  $(-\delta a, \delta a)$  or  $(-\delta \epsilon, \delta \epsilon)$   
 216 interval, with  $\delta a$  and  $\delta \epsilon$  being the step size for correlation length and RMS velocity  
 217 fluctuations respectively. In case the new value of the parameter exceeds the  
 218 boundaries defined by  $(a_{min}, a_{max})$  or  $(\epsilon_{min}, \epsilon_{max})$ , the distance  $\Delta$  to the boundary  
 219 is calculated and the new parameter value is forced to bounce back into the valid  
 220 parameter range by the same distance  $\Delta$ . The algorithm then takes model  $\mathbf{m}'$  and  
 221 uses Eqs. 9 and 7 to obtain the corresponding synthetic envelopes. In order to  
 222 decide whether to accept or reject the new model, the algorithm uses the posterior  
 223 probability exponent (Eq. 11),  $\Phi(\mathbf{m})/2$ , called here the *loglikelihood*,  $L$ , associated  
 224 with model  $\mathbf{m}$ , as an estimator of the likelihood and the goodness of the fit to  
 225 the data. Thus, if  $L(\mathbf{m})/L(\mathbf{m}') \geq 1$ ,  $\mathbf{m}'$  will be accepted. If  $L(\mathbf{m})/L(\mathbf{m}') < 1$ ,  
 226 however, it will only be accepted if  $\exp(L(\mathbf{m}) - L(\mathbf{m}')) \geq q$ ,  $q$  being a random  
 227 number between 0 and 1. This algorithm ensures that parameter values closer  
 228 to the true value have high likelihoods and are accepted more often than values  
 229 further from the true value. The acceptance rate (AR) represents the percentage  
 230 of times new parameter values were accepted through the Markov chain. There  
 231 are several criteria defining what the value of the AR should be, most of them  
 232 making assumptions about the properties of the target distributions (e.g. Brooks  
 233 et al., 2011). In our case, since we do not have any a priori information about  
 234 the posterior distributions, we aimed at AR values between 30–60 %. Finally we  
 235 calculate the 5- to 95- percentile range (PR) for each parameter in each layer in  
 236 the model from our ensemble of accepted models.

237 For more detailed descriptions of Bayesian inference and MCMC, we refer the  
238 reader to Tarantola (2005) or Brooks et al. (2011).

### 239 **2.2.2 Synthetic tests**

240 Previous studies have tested the validity of both the EFM and EFMD: Frankel and  
241 Wennerberg (1987) and Korn (1990) used a 2-D acoustic finite difference code to  
242 check the validity of their respective versions of the EFM; Korn (1997) and Hock  
243 et al. (2004) tested their approaches by obtaining synthetic seismograms from  
244 a fully elastic 2-D finite difference method and comparing them with synthetic  
245 envelopes obtained from the EFMD. Here, we tested our Bayesian inversion code  
246 with five different synthetic datasets, with varying number of layers and parameter  
247 values. Synthetic envelopes for these five models were calculated using the EFMD  
248 algorithm. Parameter values for each one are shown in Table 2, together with a  
249 summary of our synthetic tests results. In all of them, we used Pilbara Seismic  
250 Array (PSAR, Section 3) as a test array and obtained its velocity model and Moho  
251 depth from the Australian Seismological Reference Model (AuSREM, Kennett and  
252 Salmon, 2012; Kennett et al., 2013; Salmon et al., 2013b) and AusMoho model  
253 (Kennett et al., 2011) respectively, although our results should be applicable to  
254 all arrays. Based on the lower bound of the lithosphere-asthenosphere boundary  
255 (LAB) for this array (Yoshizawa and Kennett, 2015; Kennett, 2015), we set the  
256 bottom depth of all models to 200 km. Frequency bands used are listed in Table  
257 1.

258 Figures 2, 3 and 4 below, and S1 and S2 in the Supplementary Material, illus-  
259 trate the results from our synthetic tests for Models 1 to 5 (Table 2). In order to  
260 test the convergence of our algorithm, we ran three independent Markov chains for  
261 each model, with a total of 3 million iterations (parameter combinations tested)



**Table 2:** Summary of the synthetic model layering and our synthetic tests results. For each model, we include the 5–95 percentile range (PR) and the acceptance rate (AR) for each parameter, as well as the maximum loglikelihood ( $L$ ) found during the inversion.

Model	Number of layers	Layer number	Input model		Correlation length ( $a$ )		RMS velocity fluctuations ( $\epsilon$ )		Maximum $L$
			$a$ (km)	$\epsilon$ (%)	5 – 95 PR (km)	AR (%)	5 – 95 PR (%)	AR (%)	
1	1	1	5.0	5.0	4.99 – 5.05	23	4.99 – 5.00	8	-2.5
2	2	1	2.0	5.0	1.7 – 2.4	12	4.8 – 5.3	47	-0.02
		2	3.0	4.0	2.8 – 3.4		3.9 – 4.1		
3	2	1	1.0	7.0	1.00 – 1.01	51	6.95 – 7.02	47	-0.03
		2	6.0	1.0	7 – 32		1.0 – 1.8		
4	2	1	6.0	1.0	6 – 25	50	1.0 – 1.8	51	-1.3
		2	1.0	7.0	0.998 – 1.002		6.998 – 7.003		
5	3	1	1.0	4.0	1 – 23	52	0.1 – 4.7	31	-0.02
		2	2.0	3.0	1 – 21		0.6 – 6.1		
		3	4.0	2.0	3 – 30		1.8 – 3.3		

262 for the single layer model, 9 million for the 2-layer models, and 15 million for  
 263 the 3-layer model. For each chain, we discarded the models corresponding to the  
 264 burn-in phase, during which the algorithm is not efficiently sampling the posterior  
 265 probability distribution and models are still affected by the random initialization  
 266 of the Markov chain. In order to define the point at which the algorithm reached  
 267 convergence and the burn-in phase ended, we first calculated the mean loglikeli-  
 268 hood value in the second half of the chain (during which the algorithm is stable)  
 269 and then subtracted 5% off that value. We consider the algorithm has converged  
 270 the first time it accepts a model with loglikelihood  $L$  equal or higher than this  
 271 value. Our threshold was defined based on the observation, in test runs of the  
 272 EFMD, that  $L$  generally remained stable after reaching the defined threshold for  
 273 the first time.  $L$  provides an estimation of the goodness-of-fit of the synthetic data  
 274 to our real data and takes negative values, meaning fits improve as  $L$  gets closer  
 275 to zero (Eq. 11). In terms of parameter values, we consider that a narrow 5–95  
 276 percentile range (PR) points to clearly determined values of the structural param-  
 277 eters, while wide 5–95 PRs would suggest multiple parameter values are equally  
 278 likely and good at fitting our data.

279 For Model 1, with a single layer encompassing the entire lithosphere, all three

280 chains reached stability and converged within 10000 iterations. Panels d–f in Fig.  
 281 2 show our posterior probability density functions (PDFs) for each parameter, as  
 282 well as the joint PDF. In both cases, the distributions are approximately Gaus-  
 283 sian and symmetric, with the 5–95 PR being  $\sim 0.06$  km and  $\sim 0.01\%$  wide for  
 284 the correlation length and RMS velocity fluctuations respectively (Table 2), which  
 285 indicated that the range of suitable values of the parameters is very well defined.  
 286 The algorithm slightly overestimates the correlation length and underestimates the  
 287 RMS velocity fluctuations, with the input value of the parameter being included  
 288 in the 5–95 PR for the latter but not for the former (Table 2, Fig. 2). However,  
 289 the difference between the central value of the PDFs and the true value of the  
 290 parameter is  $< 0.4\%$  for both the correlation length and the RMS velocity fluc-  
 291 tuations. Graphs on the right hand side of Fig. 2 (panels g–n) show histograms  
 292 of the synthetic envelopes for our ensemble of accepted models for all frequency  
 293 bands. As frequency increases, both envelope amplitudes and width of the ensem-  
 294 ble of synthetic envelopes increase too. However, in all cases, the highest density  
 295 of envelopes, indicated by a dark brown color, is found in a very narrow line that  
 296 matches the input data envelopes, not only in the time window used for the fit  
 297 (shadowed area in the plots), but also outside of it.

298 Model 2 contains two layers, representing the crust and lithospheric mantle.  
 299 Our three chains converged in less than 120000 iterations and remained stable for  
 300 the rest of the inversion, as shown in panels a–c in Fig. 3. Panels d–i in this figure  
 301 summarise our results. In this case, the PDFs for the parameters in both layers  
 302 are narrow (the 5–95 PR is  $< 0.7$  km wide at most for  $a$  and  $< 0.5\%$  for  $\epsilon$ ) and  
 303 approximately centered around the input values, even if they are not Gaussian and  
 304 show some local maxima. The true values of the parameters lie within the 5–95  
 305 PR in all cases, near the center of the joint PDFs, and the maximum difference

306 between the input values and the absolute maxima of the PDFs is 2%. Panels j–q  
 307 in Fig. 3 indicate fits to the synthetic data are good, since they show again that  
 308 the largest concentration of synthetic envelopes for all frequencies coincides with  
 309 the input data envelopes.

310 Models 3 and 4 have the same interface structure as model 2 (Table 2) and  
 311 investigate high contrast situations in which a strong heterogeneity layer is above  
 312 or below a layer containing weak heterogeneities respectively. Figs. S1 and S2  
 313 summarise our results and can be found in the Supplementary Material. In both  
 314 cases, the chains reached stability within 11000 iterations. Posterior PDFs for the  
 315 strongly scattering layer are approximately Gaussian and narrow for both models  
 316 3 and 4, with maxima that deviate from the input parameter values by 0.4%  
 317 at most (Table 2). The weakly scattering layer, however, is poorly resolved for  
 318 both models. The posterior PDFs for this layer are very similar in both cases  
 319 and clearly non-Gaussian. They show multiple maxima that do not correspond  
 320 to the input parameter values, which widens the 5–95 PR, especially for  $a$ . The  
 321 RMS velocity fluctuation values seem to be constrained to the range from 0.5–  
 322 1.9 % for both models, while the shape of the PDFs suggests any value of the  
 323 correlation length would be equally acceptable, even if large values ( $> 5$  km) are  
 324 favoured. The stability of the chains, shown in panels a–c in Figs. S1 and S2,  
 325 together with the ensemble of synthetic envelopes on panels j–q, indicate that all  
 326 these models provide similarly good fits to the data and have similar loglikelihoods.  
 327 This observation points to solutions being highly non-unique, and to the scattering  
 328 parameters of the weakly heterogeneous layer not being easily recoverable for these  
 329 high contrast cases.

330 Finally, model 5 contains three layers, with boundaries corresponding to upper  
 331 and lower crust and lithospheric mantle. Our results are shown in Figs. 4 and

332 Table 2. Chains converged in less than 130000 iterations. In all cases, PDFs  
333 are clearly non-Gaussian (panels d-l on Fig. 4) and have complex shapes, which  
334 widens the 5–95 PR and increases the range of suitable values of the parameters.  
335 The correlation length PDFs show clearly defined maxima near the true values of  
336 the parameter in all layers (the maximum distance between the maximum and the  
337 input parameter value being 0.35%). RMS velocity fluctuations PDFs are more  
338 complex and neither of them show clear maxima near the input parameter values.  
339 Figure S3 contains the marginal PDFs for all parameters in all layers, as well  
340 as the PDF for each individual parameter. It shows a strong trade-off between  
341 parameter values in different layers of the model, especially the two crustal layers,  
342 and allows us to identify two independent sets of parameters from our results (see  
343 Section S.1 in the Supplementary Material for details). This interaction between  
344 the parameters is caused by two main factors: first, the energy balance the EFMD  
345 is based on (Eq. 9) is strongly dependent on the layering of the model, since  
346 the maximum energy that can be present within a layer at any time depends on  
347 its thickness (i.e. energy leaks out of thinner layers faster); second, correlation  
348 length values have a much smaller effect on coda amplitudes, compared with RMS  
349 velocity fluctuations, so the algorithm uses  $\epsilon$  to compensate the excess or lack of  
350 energy within a layer and match data coda amplitudes. Since panels m–t on Fig.  
351 4 do not show two clearly different sets of envelopes in our ensemble of synthetic  
352 envelopes, and given that the loglikelihood values remained stable throughout the  
353 three independent chains we ran for this example, we conclude that both sets of  
354 parameters we obtained from our inversion provide equally good fits to the data,  
355 even if neither of them match our input parameter values.

356 Overall, our results show that our Bayesian algorithm is capable of successfully  
357 fitting our data and retrieving the input parameter values for our 1-layer and 2-

358 layer models. For our 3-layer model, however, the method provides good fits  
359 to the data but fails to obtain the correct parameter values, so we cannot trust  
360 results from this model for real data inversions, since we do not know what the  
361 scattering parameters are beforehand. Our observations illustrate the usefulness  
362 of the Bayesian approach we took in this study. It provides detailed information  
363 about the parameter space and indicates whether a single set of parameters that fits  
364 our data exists or a range of models can equally match the data. Any estimation  
365 of scattering parameters in a maximum-likelihood framework would therefore have  
366 led to erroneous conclusions about the physical parameters in this system, which  
367 we have avoided. The joint PDFs highlight the complicated relationships and  
368 trade-offs between the model parameters in the different settings explored here,  
369 which had not been observed in previous studies using the EFMD. We do not  
370 observe systematic overestimation of  $a$  in the EFMD, as reported by Hock et al.  
371 (2004). This observation might be related to the limited number of models tested  
372 in grid search approaches and the observed trade-offs between parameters.

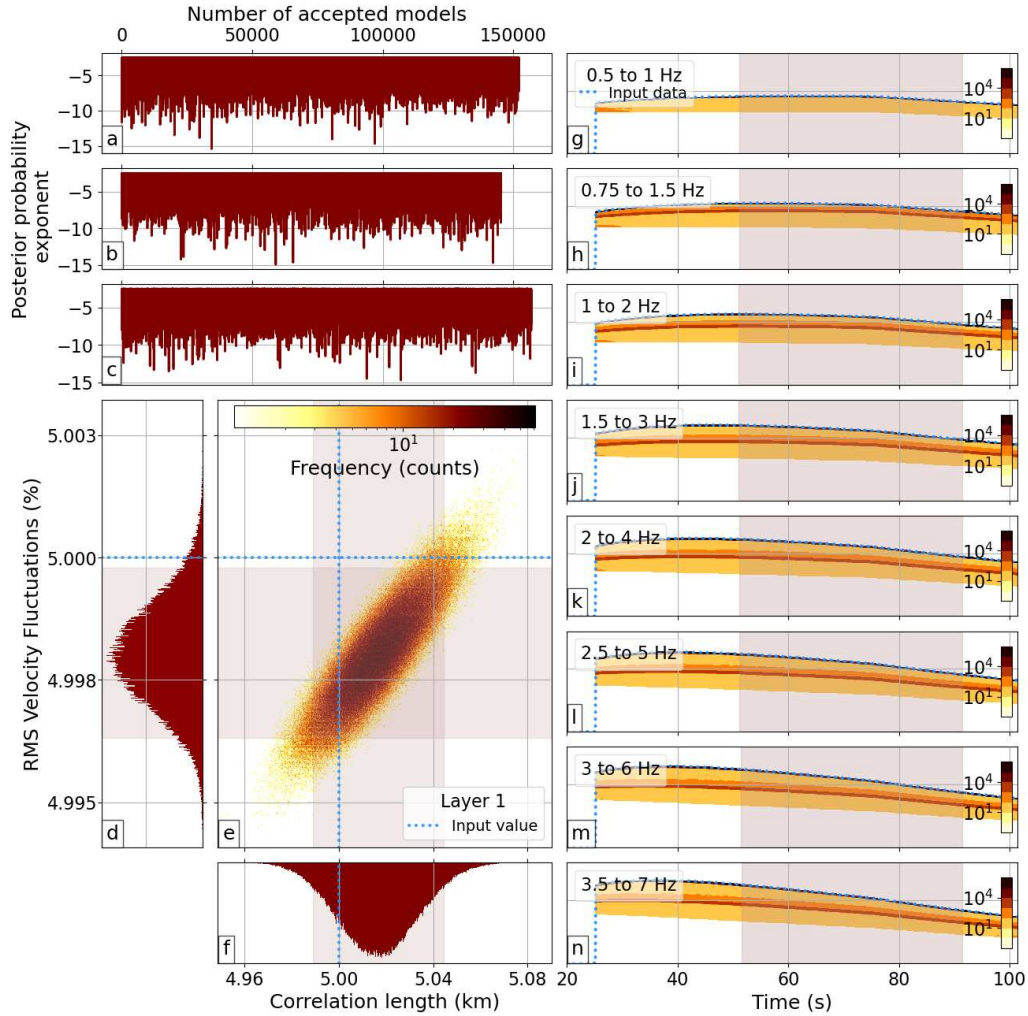


Figure 2: Summary of the results obtained from our EFMD algorithm for synthetic model 1 from Table 2 from three separate chains, adding up to a total of 3 million iterations (parameter combinations tested). Panels a–c show the loglikelihood (or posterior probability exponent) for each accepted model in the chain, once the burn-in phase was removed. Panels d–f contain the posterior PDFs of the structural parameters, as well as the joint PDF. Dotted blue lines in these plots represent the input parameter values and the shaded area corresponds to the 5–95 percentile range (PR). Panels g–n on the right show 2D histograms of the synthetic envelopes for all accepted models and frequency bands, with color bars indicating the number of models that produced a data sample within each bin. Vertical scale is the same in all plots. The shaded area here indicates the time window used for the fitting and blue dotted lines are the input data.

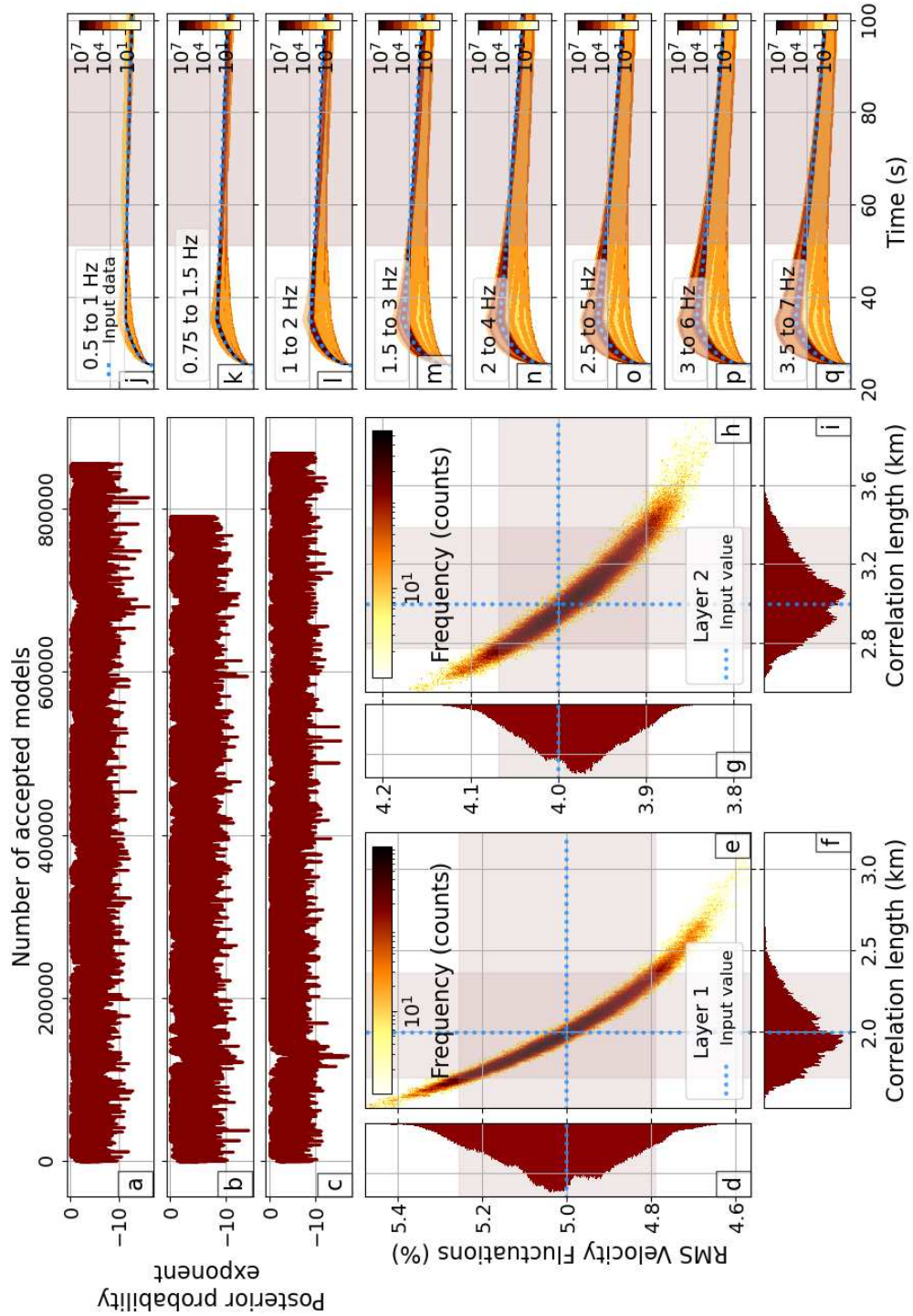


Figure 3: As Fig. 2 but for synthetic model 2 from Table 2 (2-layer model).

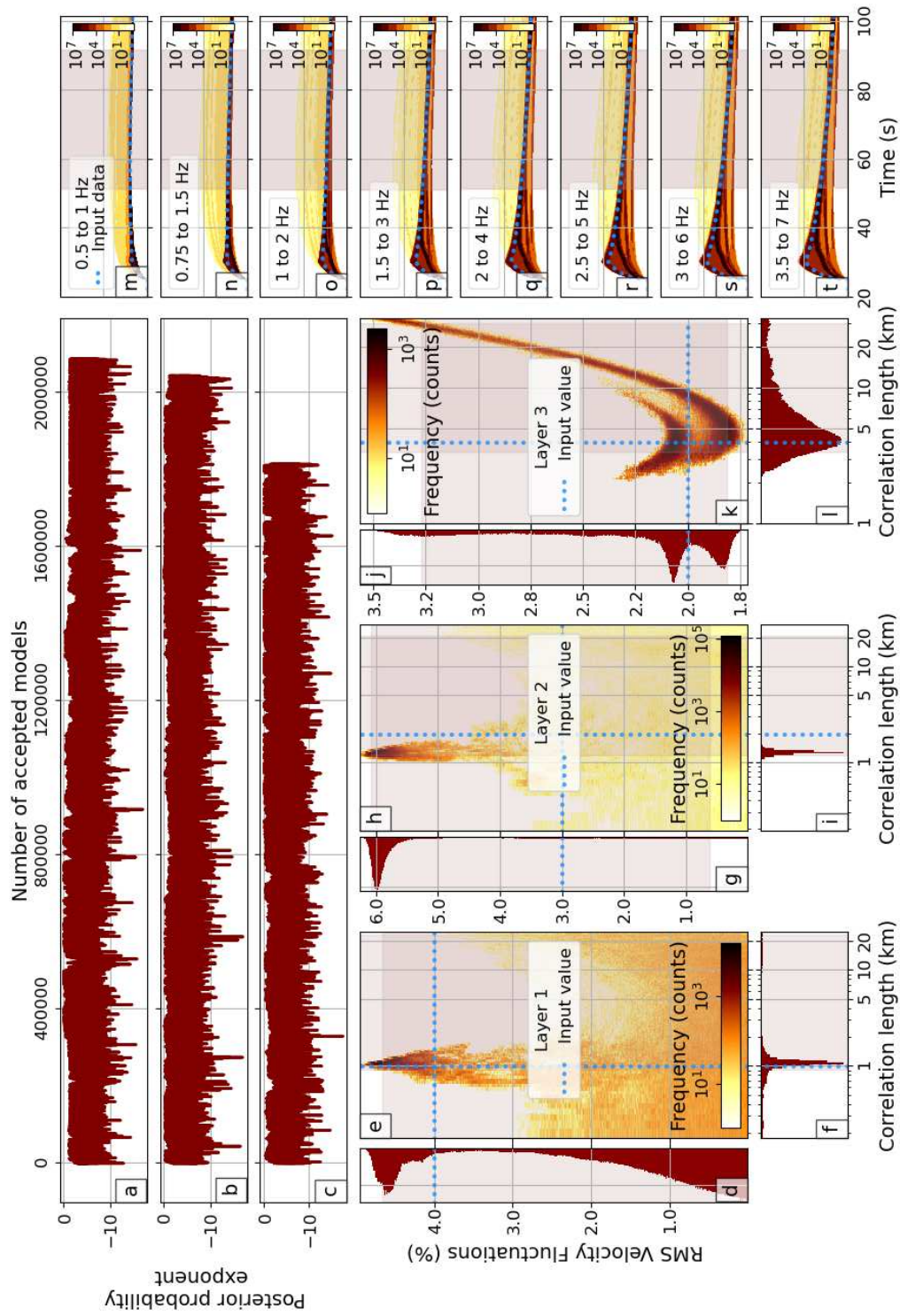


Figure 4: As Fig. 2 but for synthetic model 5 from Table 2 (3-layer model).



**Table 3:** Number of events and good quality (SNR > 5) traces for each array and frequency band.

		Number of events per frequency band							
		0.5–1 Hz	0.75–1.5 Hz	1–2 Hz	1.5–3 Hz	2–4 Hz	2.5–5 Hz	3–6 Hz	3.5–7 Hz
PSAR	Events	86	161	213	276	343	268	212	158
	Traces	973	1899	2489	3226	3179	2965	2282	1641
WRA	Events	292	355	385	407	413	410	412	406
	Traces	709	843	916	977	983	984	980	965
ASAR	Events	309	375	440	429	405	397	386	374
	Traces								

### 373 **3 DATA SELECTION AND PROCESSING**

374 Our dataset consists of seismic recordings from teleseismic events from January  
 375 1, 2012 to December 31, 2018, and with epicentral distances between 30 and 80  
 376 degrees from the arrays, with source depths greater than 200 km and magnitudes  
 377 from 5 to 7. These conditions ensure vertical or nearly vertical incidence angles and  
 378 prevent near-source scattering and unwanted deep seismic phases from appearing  
 379 in our time window of interest.

380 After removing the instrument response, we calculate the signal-to-noise ratio  
 381 (SNR) for each trace and frequency band using the peak-to-peak amplitude in two  
 382 separate time windows: for noise, we used a 20 s long window, starting  $\sim 25$  s  
 383 before the theoretical P-wave arrival (as estimated from PREM (Dziewonski and  
 384 Anderson, 1981)), while for the signal we chose a time window starting 1 second  
 385 before the theoretical first arrival and ending 40 seconds later. Only traces with  
 386 signal-to-noise ratio equal to or higher than 5 were used.

387 Hock et al. (2004) pointed out that the EFMD generally overestimated the  
 388 RMS velocity fluctuations by up to 3% when using only vertical-component data  
 389 and that a mix of 1-component and 3-component data produced unstable results,  
 390 both of them caused by the difference in coda amplitudes between 1-component  
 391 and 3-component data. However, the International Monitoring System arrays

392 are dominantly vertical component, with WRA having three 3-component sta-  
 393 tions and ASAR a single 3-component central station. All PSAR stations are  
 394 three-component. To address this issue, we tried calculating a correction factor to  
 395 approximate 1-component to 3-component coda levels. We used several different  
 396 approaches to obtain this correction factor, all of them based on the ratio be-  
 397 tween every available 3-component coda envelope  $A(t; \omega_c)$  or normalised envelope  
 398 (left hand side on Eq. 7) and its 1-component (vertical) counterpart. However, we  
 399 found that these ratios varied significantly from event to event and frequency band  
 400 to frequency band and followed complicated probability distributions, even after  
 401 using our large datasets to calculate them. The corrected 1-component envelopes  
 402 did not, in general, fully match the 3-component coda amplitudes using this ap-  
 403 proach. Our tests also showed the correction factors needed for the normalised  
 404 envelopes were different than for the unnormalised ones and that small variations  
 405 in coda amplitudes affected the results we got from both the EFM and EFMD.  
 406 We also used the “corrected” 1-component data in our EFM-EFMD algorithm  
 407 and compared the results in different settings with those from our 3-component  
 408 data for PSAR. In both cases, the distribution of the heterogeneity followed simi-  
 409 lar patterns, but the values of the scattering parameters and the posterior PDFs  
 410 differed. Therefore, we only analyse 3-component data in this study.

411 Table 3 shows the number of events and traces used for each array and fre-  
 412 quency band. For PSAR, we only kept events with 5 or more good quality 3-  
 413 component traces. For WRA and ASAR, we used all available 3-component data.  
 414 This allowed us to test this method with different station configurations, from a  
 415 full array (PSAR) to a small group of stations (WRA) or even a single station  
 416 (ASAR). In all cases, our large event dataset guarantees a thorough sampling of  
 417 the structure beneath the stations and allows us to obtain robust results.

418 For each array, the data processing prior to the EFM/EFMD analysis was  
 419 carried out as follows:

420 (i) Computation of 3-component envelopes for each frequency band, station and  
 421 event. All traces were trimmed to the time window going from  $t_N$  seconds  
 422 before to  $3t_N$  seconds after the theoretical P wave arrival ( $t_N$  being the travel  
 423 time through the lithosphere,  $\sim 25$  s for all arrays). These were then stacked  
 424 by event, normalised using Eq. 7 and stacked by frequency band. Unnor-  
 425 malised envelopes for all events were also stacked by event and frequency  
 426 band. The variance of both normalised and unnormalised envelopes was cal-  
 427 culated sample by sample from all individual event stacked envelopes and  
 428 used as the uncertainty of our data.

429 (ii) Estimation of  $Q_s$ ,  $Q_i$ ,  $Q_{diff}$ ,  $a$  and  $\epsilon$  for a single scattering layer using the  
 430 EFM.

431 (iii) Bayesian inversion for the structural parameters of each layer in each model  
 432 type from Fig. 5 by applying the envelope modelling technique from EFMD,  
 433 as described in Section 2.2, and using the  $Q_i$  values obtained from the single  
 434 layer EFM. The bottom depth of these models was set to 200 km in all cases  
 435 to make it easier to compare our results from the three arrays. In order to  
 436 speed up this process, our data were resampled to a common sampling rate  
 437 of 10 Hz (original sampling rates were 40 Hz for PSAR and WRA and 20 Hz  
 438 for ASAR) before applying the EFMD algorithm.

439 Background lithospheric P-wave velocities (Fig. 5) and Moho depths for each  
 440 seismic array were obtained from the Australian Seismological Reference Model  
 441 (AuSREM, Kennett and Salmon, 2012; Salmon et al., 2013b; Kennett et al., 2013;  
 442 Salmon et al., 2013a) and AusMoho model (Kennett et al., 2011) respectively.

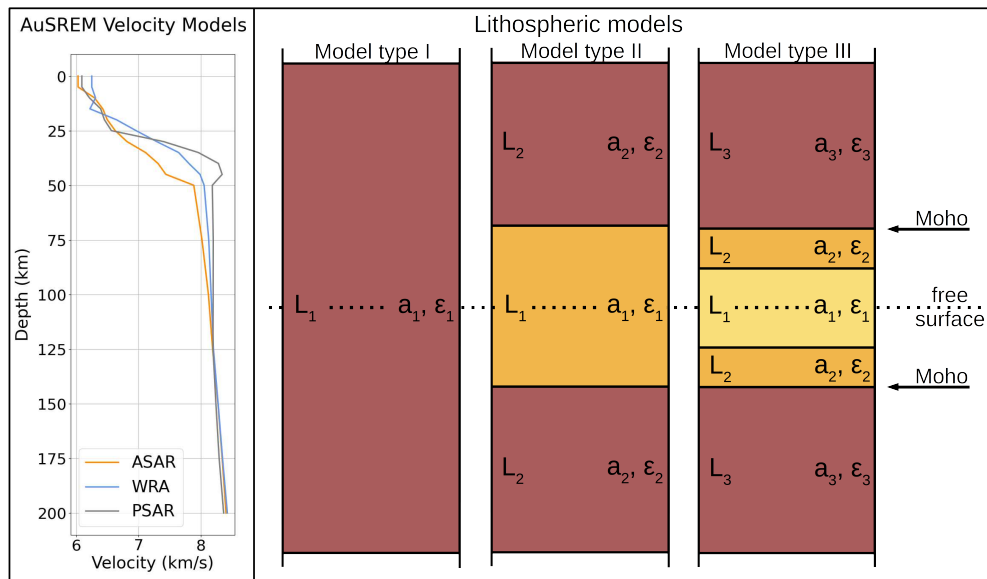


Figure 5: Representation of the AuSREM P-wave velocity models for each seismic array (left) and the three types of lithospheric models used in the EFMD (right). The layering and bottom depth is the same we used in the models for our synthetic tests, with Model types I, II and III corresponding to Models 1, 2 and 5 from Table 2 (Models 2, 3 and 4 have the same layering). Moho depths for each array were obtained from the AusMoho model (Kennett et al., 2011).

443 **4 TECTONIC SETTING**

444 ASAR and WRA are located on the North Australian Craton (NAC), one of the  
445 Proterozoic cratons in the Precambrian westernmost two-thirds of the Australian  
446 continent (e.g. Myers, 1990; Simons et al., 1999; Cawood and Korsch, 2008; Well-  
447 man, 1998) (Fig. 6). The NAC consists of late Archaean to Proterozoic cratonic  
448 blocks overlaid by Proterozoic and Phanerozoic orogenic belts and basins. PSAR  
449 is located on Archaean lithosphere part of the West Australian Craton (WAC),  
450 which includes both the Pilbara and Yilgarn Archaean cratons, as well as some  
451 Proterozoic orogens and basins (Cawood and Korsch, 2008) (Fig. 6). Present day  
452 tectonic activity in Australia is concentrated along the active plate boundaries in  
453 the north and east, with continental regions presenting only moderate seismicity  
454 (Fichtner et al., 2009).

455 Previous studies have investigated crust and lithospheric thicknesses and struc-  
456 ture around the three arrays studied here. Thick crust ( $L_c > 40$  km) with a wide  
457 and smooth Moho transition has generally been found in the Proterozoic shields  
458 of Central Australia while the Archaean regions of western Australia have thinner  
459 crust ( $L_c < 40$  km) and sharper crust-upper mantle transitions (e.g. Clitheroe  
460 et al., 2000; Sippl, 2016; Salmon et al., 2013a; Kennett et al., 2011; Kennett and  
461 Saygin, 2015). This difference in crustal thickness between Archaean and Pro-  
462 terozoic regions seems not to fit the trend of crustal thickness increasing with age  
463 suggested for Australia (e.g. Clitheroe et al., 2000). It has been attributed to post  
464 Archaean tectonic activity underplating material at the base of the crust in these  
465 regions, as opposed to the Archaean cratons being located at passive margins and,  
466 therefore, not being affected by more recent tectonics (e.g. Drummond and Collins,  
467 1986).

468 Sippl (2016) and Kennett and Sippl (2018) imaged a series of Moho offsets

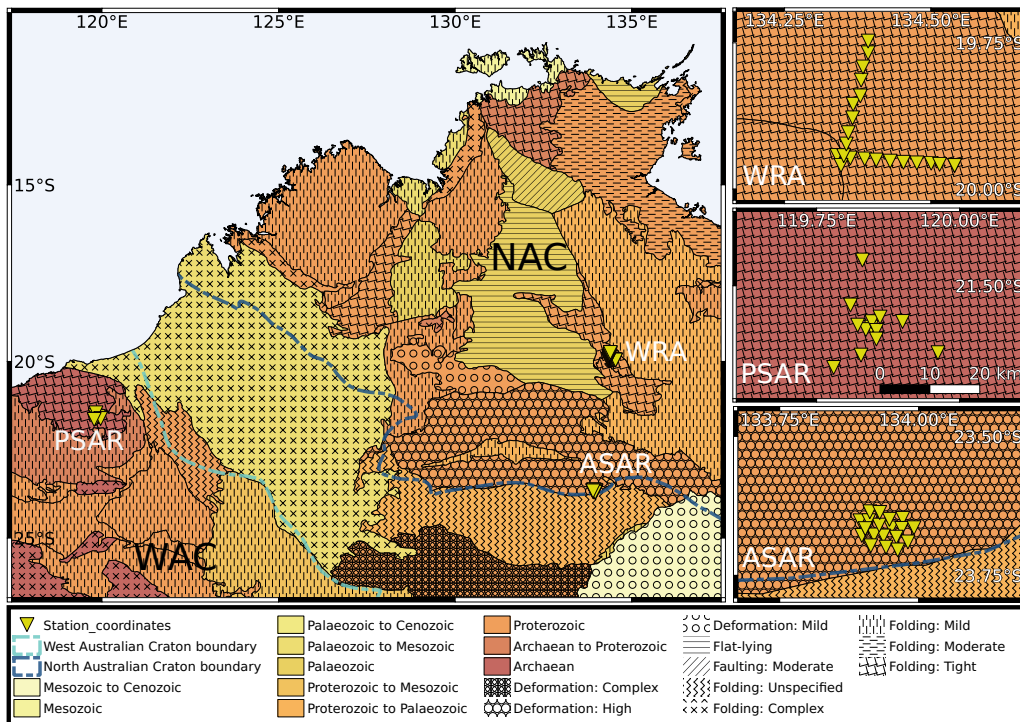


Figure 6: Simplified geological map of northwestern Australia and location of the three seismic arrays used in this study (Alice Springs Array (ASAR), Warramunga Array (WRA) and Pilbara Seismic Array (PSAR)). Blue dashed lines represent the boundary of the West Australian Craton (WAC, light blue line) and the North Australian Craton (NAC, dark blue line). PSAR and WRA are located on Archaeal and Proterozoic basement respectively, inside the cratons, while ASAR is situated at the southern boundary of the NAC. Panels on the right show the station configuration of the arrays, with the same scale bar shown for PSAR being applicable to all three maps. Geological structure based on Blake and Kilgour (1998) and Raymond et al. (2018).

469 along a north-south profile in the NAC. One of these offsets is associated with the  
 470 Redbank Shear Zone, which separates the Aileron Province and the location of  
 471 ASAR from the Amadeus Basin, just south of the array (e.g Goleby et al., 1989;  
 472 Korsch et al., 1998; Sippl, 2016). The profile used in Sippl (2016) and Kennett and  
 473 Sippl (2018) is located roughly 50 km west of ASAR and shows an offset of up to 20  
 474 km coinciding with ASAR latitude, even though they show constant Moho depths  
 475 beneath the array. An east-west gravity anomaly has been found at the location of

476 this Moho offset (Sippl, 2016, Fig. 1) and attributed to denser lithosphere at the  
 477 base of the crust caused by the uplift of the Aileron crustal block during the Alice  
 478 Springs Orogeny 400–350 Ma ago (Goleby et al., 1989; Aitken, 2009; Aitken et al.,  
 479 2009; Sippl, 2016). Another offset imaged by Sippl (2016) and Kennett and Sippl  
 480 (2018), further north, shows a north-south decrease in Moho depth of about 10 km  
 481 just south from WRA, which has been associated with a Proterozoic suture zone.  
 482 Corbishley (1970) also found evidence of a layered and dipping structure below  
 483 WRA. Gravimetric data do not show any anomalies here (Sippl, 2016), which has  
 484 been attributed to a layer of sediments near the surface isostatically compensating  
 485 the mass excess at depth.

486 Several studies have addressed the thickness of the lithosphere beneath the  
 487 Australian continent. Some suggest similarly deep interfaces across all Precam-  
 488 brian cratonic regions in Australia ( $L_l \approx 200$  km) (e.g. Debayle and Kennett,  
 489 2000). More recent studies use a lithosphere-asthenosphere transition zone (LAT),  
 490 defined as a mechanical or thermal boundary layer related to changes in rheology,  
 491 as opposed to a simple interface at the bottom of the lithosphere (e.g. Kennett and  
 492 Sippl, 2018; Yoshizawa and Kennett, 2015). Specifically, Kennett and Sippl (2018)  
 493 place the upper and lower bounds of the LAT at 140 and 170 km depth respec-  
 494 tively for ASAR, and at 120 and 160 km for WRA, while Yoshizawa and Kennett  
 495 (2015) place them at 100 and 200 km depth for PSAR. Some studies have also  
 496 found evidence for mid-lithospheric discontinuities below both ASAR and WRA  
 497 which have been interpreted as vertical variations in mantle composition, grain  
 498 size or fabric, for example a low velocity melt cumulate layer (Ford et al., 2010)  
 499 and as a former mantle detachment zone associated with the Alice Springs orogeny  
 500 (Kennett and Sippl, 2018).

**Table 4:** Summary of the main results obtained from the EFM for all arrays: intrinsic ( $Q_{i0}$ ) and diffusion ( $Q_{d0}$ ) quality factors values at 1 Hz, intrinsic quality factor frequency dependence coefficient ( $\alpha$ ), correlation length ( $a$ ) and RMS velocity fluctuations ( $\epsilon$ ).

Array	$Q_{i0}$	$Q_{d0}$	$\alpha$	$a$ (km)	$\epsilon$ (%)
PSAR	$2100 \pm 200$	$500 \pm 40$	0.0	$0.9 \pm 0.1$	$2.9 \pm 0.1$
WRA	$2100 \pm 100$	$400 \pm 20$	0.0	$1.1 \pm 0.1$	$4.5 \pm 0.1$
ASAR	$1000 \pm 100$	$400 \pm 40$	0.2	$0.9 \pm 0.2$	$4.7 \pm 0.2$

## 501 5 RESULTS AND DISCUSSION

### 502 5.1 EFM results

503 We calculated the coda decay rate,  $a_1$ , and its value at zero time,  $a_0$ , for all  
504 frequency bands and arrays as stated in Section 2.1. We applied the linear least-  
505 squares fit of the squared stacked envelopes at the free surface (Fig. S4) to a time  
506 window starting  $t_N$  s after the theoretical P wave arrival ( $t_N$  being the one-way  
507 travelttime through the lithosphere), since the EFM is only applicable after the  
508 direct wave has left the scattering layer (Korn, 1990; Hock and Korn, 2000). The  
509 length of this time window varied from 42.5 to 48 s for all arrays and frequency  
510 bands, depending on differences in P wave velocities and arrival times. Table 4  
511 and Figure 7 summarise our EFM results for all arrays.

512 A least-squares fit using Eq. 2 then allowed us to calculate the quality factors  
513 for diffusion and anelasticity at 1 Hz from  $a_1$ . For all arrays, the coda decay rate for  
514 the lowest frequency band did not follow the trend defined by the other frequency  
515 bands. Including it in the least squares fit produced inconsistent results, and it  
516 was excluded from the analysis (Fig. S5). The intrinsic quality factor,  $Q_i$ , takes  
517 similar, frequency independent ( $\alpha = 0$ ), values of  $\sim 2000$  for WRA and PSAR. For  
518 ASAR, our best fits to the coda decay rate (Eq. 2) correspond to  $\alpha = 0.2$  (Fig.  
519 S5) and  $Q_i \sim 1000$ . Diffusion quality factor values at 1 Hz are similar for ASAR



520 and WRA ( $\sim 400$ ), and higher for PSAR ( $\sim 500$ ). Since this quality factor does  
 521 not depend on  $\alpha$  (Eq. 16, Korn (1990)), this translates into  $Q_{diff}$  following the  
 522 same trend for all arrays but being higher for PSAR than for WRA and ASAR.

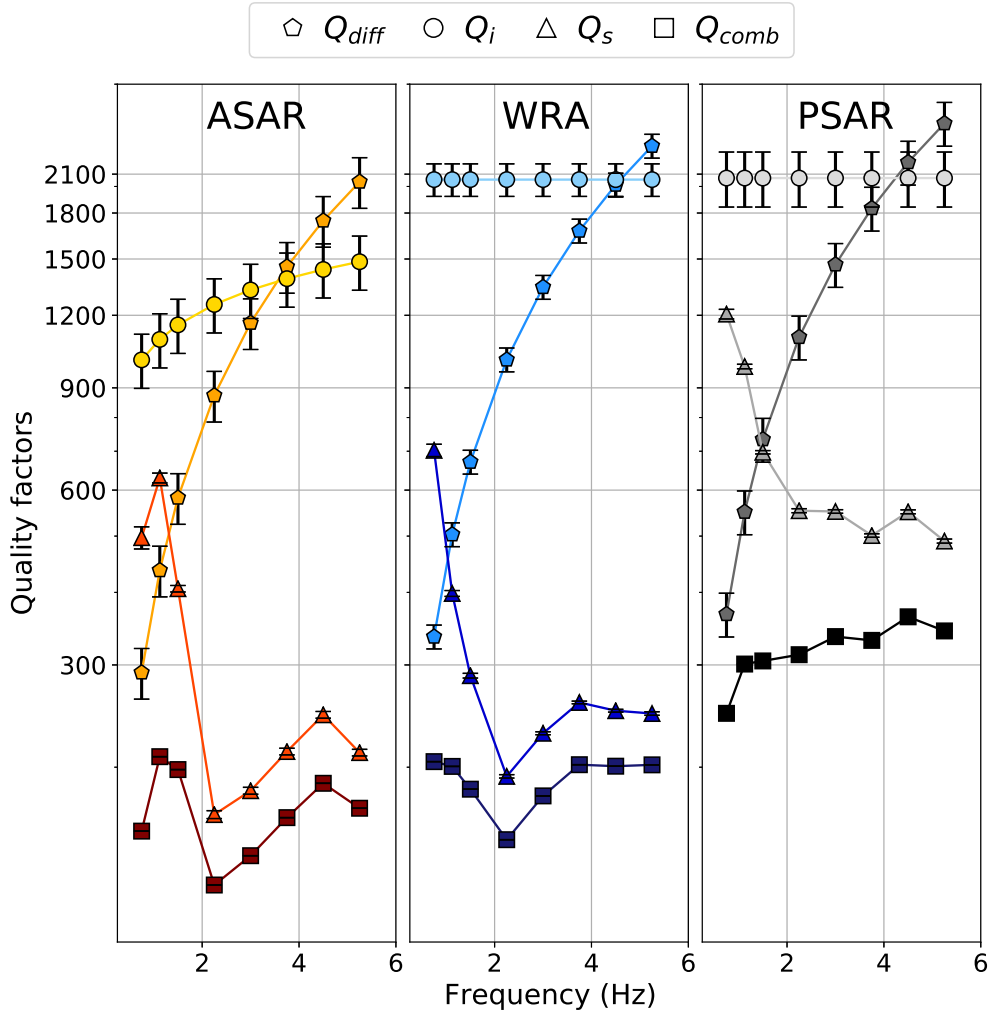


Figure 7: Frequency dependence of the intrinsic ( $Q_i$ ), the diffusion ( $Q_{diff}$ ), scattering ( $Q_s$ ) and combined ( $Q_{comb}$ ) quality factors for all arrays.

523 Figure S6 shows measured  $Q_s$  values, obtained from Eq. 5, together with the  
 524 theoretical least-squares regression curves derived by Fang and Müller (1996) for  
 525 the relationship between the structural parameters and  $Q_s$  for an exponential ACF.

526 As explained on Section 2.1, these parameters represent a first approximation to  
 527 the average spatial distribution and strength of the heterogeneity of a hypothetical  
 528 single scattering layer beneath the arrays. Correlation length values are similar for  
 529 the three arrays, varying from 0.92 – 1.1 km. Heterogeneities appear to be weaker  
 530 beneath PSAR than ASAR or WRA, with  $\epsilon$  jumping from  $\sim 3.0\%$  for PSAR to  
 531  $\sim 4.5\%$  and  $\sim 4.7\%$  for WRA and ASAR respectively.

532 Figure 7 shows the frequency dependence of the different quality factors ob-  
 533 tained from the EFM. The total quality factor,  $Q_{comb}$ , and  $Q_s$  follow a similar  
 534 trend. They take the highest and lowest values for PSAR and ASAR respectively.  
 535 For WRA and ASAR, their maximum value corresponds to the 0.5–1 and 0.75–1.5  
 536 Hz bands respectively, and the minimum for the 1.5–3 Hz frequency band. The  
 537 frequency dependence of  $Q_s$  and  $Q_{comb}$  for the highest frequencies is similar for  
 538 both arrays. This indicates that the dominating scale length of the heterogeneity  
 539 is in the 2.6–5.3 km range for these arrays when we consider a single scattering  
 540 layer. For PSAR, however,  $Q_s$  decreases for frequencies below 1.5 Hz and then re-  
 541 mains approximately constant, which could be indicative of different scale lengths  
 542 of the heterogeneity being equally present in the structure. For this array,  $Q_{comb}$   
 543 increases slowly over the frequency range covered here.

544 In general, diffusion is the strongest attenuation mechanism (lowest Q) at low  
 545 frequencies, with scattering dominating at higher frequencies. For WRA, this  
 546 transition happens at 0.75 Hz, while for ASAR and PSAR, the change takes place  
 547 at 1.125 Hz. Anelasticity remains the weakest attenuation mechanism (highest Q)  
 548 at low frequencies, up to 4.5 Hz for WRA and PSAR and 3.75 Hz for ASAR. Above  
 549 that frequency,  $Q_{diff}$  becomes dominant. These results agree with the observations  
 550 by Korn (1990), who obtained  $Q_i > 1000$  and  $Q_{diff} \sim 300 - 400$  at 1 Hz for WRA,  
 551 even if his results showed that  $Q_i$  remained larger than  $Q_{diff}$  up to 10 Hz. Our

552  $Q_{comb}$  results suggest that, even if  $Q_s$ ,  $Q_i$  and  $Q_{diff}$  are lower at most frequencies  
 553 for ASAR than for the other two arrays, total attenuation strength is similar  
 554 for ASAR and WRA. These lower  $Q_{comb}$  values could be related to the location  
 555 of these arrays on the NAC, younger in origin than the WAC (Section 4). The  
 556 location of ASAR, on the southern edge of the NAC, in an area widely affected by  
 557 the accretionary processes that took place during the assembly of the Australian  
 558 continent, as well as major events like the Petermann and Alice Springs orogens  
 559 (Section 4), could explain the lower values of the different quality factors obtained  
 560 for this array. For PSAR, the generally high quality factors values we obtained  
 561 could be related to the location of the array on a tectonically quiet Archaean  
 562 craton (Section 4). Previous studies (e.g. Cormier, 1982; Korn, 1993; Sipkin and  
 563 Revenaugh, 1994; Domínguez and Rebolgar, 1997) have also found lower Q values  
 564 in regions with quiet tectonic histories, an observation that matches our results  
 565 from the EFM for all three arrays.

## 566 **5.2 EFMD results**

567 We used the 1-layer and 2-layer lithospheric models shown in Fig. 5 in our inversion  
 568 of the data for all three arrays.  $Q_i$  values necessary to calculate the synthetic  
 569 envelopes from Eq. 7 are determined by the EFM. As with our synthetic tests,  
 570 we ran three parallel Markov chains for each array and model type, with 1 million  
 571 or 3 million iterations for models with 1 and 2 layers respectively. The burn-in  
 572 phase, defined as described in section 2.2.2, was removed from all chains. Table 5  
 573 summarises our results. To avoid repetition, we include here only the most relevant  
 574 results for each array. Figures from the rest of our inversions can be found in the  
 575 Supplementary material.

576 Inversion of PSAR data with Model type I (single layer), revealed this model

577 produces very large amplitude codas that barely decay over time (Fig. S7). All  
 578 chains were stable and converged within 14000 iterations, but the maximum log-  
 579 likelihood reached during the inversion ( $< -10^6$ , panels a-c on Fig. S7), indicated  
 580 fits to the data are very poor, which is also obvious from the comparison of the  
 581 ensemble of synthetic envelopes with the data (panels g-n on Fig. S7). The poste-  
 582 rior PDFs suggest a nearly homogeneous lithosphere, with  $\epsilon \sim 0\%$  and  $a > 20$  km.  
 583 This is likely due to the large thickness of the layer (200 km) preventing diffusion  
 584 out of it and, therefore, energy levels in the heterogeneous layer remaining high at  
 585 all times, regardless of the magnitude of the scattering parameters. We also tested  
 586 model type I on ASAR data, since coda levels for this array are higher. These  
 587 results are shown on Fig. S8. Despite the higher coda amplitudes, model type I  
 588 fails to fit our data for this array, with the maximum loglikelihood reached being  
 589 on the order of  $-10000$ . ASAR coda amplitudes are similar to WRA, indicating  
 590 similar behaviour. Therefore, this model was not tested for WRA.

591 Model type II (two layer) inversions for all three arrays showed much better  
 592 fits for frequency bands D-H (Table 1) than for A-C (example for PSAR in Fig.  
 593 S9). However, loglikelihood values are still very low ( $< -4 \times 10^5$ ), Table 5), which  
 594 indicates poor fits to the data and, therefore, unreliable parameter estimations,  
 595 even if there is a substantial improvement with respect to model type I. Our EFM  
 596 results show scattering only becomes the dominant attenuation mechanism above  
 597 1.5 Hz for PSAR (Fig. 7). This, together with coda amplitudes shown on panels  
 598 j-q in Fig. S9 being barely above the noise level in the time window of interest  
 599 for the lowest frequency bands, suggests these codas are affected by large-scale  
 600 heterogeneities and might not be composed only of energy scattered at small-scale  
 601 structure. Therefore, the EFMD may not be able to fit our coda envelopes for  
 602 frequencies below this threshold. To test this, we ran our EFMD inversion code

**Table 5:** Summary of our EFMD results for all arrays and model types.

Array	Model type	Frequency bands	Layer number	Correlation length ( $a$ )		RMS velocity fluctuations ( $\epsilon$ )		Maximum $L$
				5-95 PR (km)	AR (%)	5-95 PR (%)	AR (%)	
PSAR 3 comp.	I	A-H	1	23 – 32	48	< 0.01	47	< $-14 \times 10^6$
	II	A-H	1	0.5 – 25	75	< 0.01	47	< -450000
			2	0.5 – 32		< 0.01		
	II	D-H	1	0.5 – 0.8	59	2.3 – 2.5	44	-7.1
2			4 – 32	0.1 – 1.8				
ASAR	I	A-H	1	2 – 30	93	0.01 – 0.07	44	-10500
	II	D-H	1	0.2 – 1.4	59	2.4 – 3.0	50	-2.2
2			3 – 32	0.1 – 3.7				
WRA	II	D-H	1	0.7 – 1.5	60	3.1 – 3.9	53	-0.7
			2	3 – 32		0.2 – 5.0		

603 for frequency bands D to H (Table 1) alone. By comparing our results for PSAR  
 604 in Fig. S9 and Fig. 8, we observe considerable improvement in the fits to the  
 605 data, also evidenced by much higher loglikelihood values ( $< -10$ ). Given these  
 606 new observations, we discard frequency bands A to C (central frequencies below  
 607 1.5 Hz, Table 1) in future inversions of the data for all arrays.

608 Figures 8, 9 and 10 summarise our results for all three arrays and model type  
 609 II. All Markov chains converged within 10000, 7000 and 4000 iterations for PSAR,  
 610 ASAR and WRA, respectively. The scattering structure beneath all three arrays  
 611 shows different amounts of heterogeneity in the crust and a relatively homogeneous  
 612 lithospheric mantle. The posterior PDFs for both parameters in the top layer in  
 613 all cases are roughly Gaussian and narrow (Table 5). Maxima for the correlation  
 614 length PDFs for PSAR, ASAR and WRA are at 0.6, 0.7 and 1 km, while RMS  
 615 velocity fluctuations posteriors peak at 2.4%, 2.7% and 3.6% respectively. PDFs  
 616 for layer 2, on the other hand, show no clear maxima and also have similar shapes  
 617 for all arrays. For PSAR,  $\epsilon$  only takes values below  $\sim 3\%$ , while for WRA and  
 618 ASAR, the PDF extends up to  $\sim 8\%$  and  $\sim 6\%$  respectively. In all cases, most  
 619 of the accepted models have  $\epsilon < 1\%$ . The correlation length PDF, on the other  
 620 hand, extends throughout the entire parameter space. For PSAR and WRA, large  
 621 values of  $a$  ( $> 5$  km) are favoured, while small correlation lengths ( $< 1$  km) seem

622 to work better for ASAR. Loglikelihood values are high ( $> -10$ ) for all arrays,  
623 which suggests fits to the data are generally good. The shape of the PDFs for  
624 the bottom layer makes our solutions non-unique and highlights a complicated  
625 trade off between the scattering parameters. These results strongly resemble the  
626 ones we obtained from our synthetic test of model 3 (Table 2), in which our  
627 Bayesian inference algorithm successfully recovered the input parameter values  
628 for the strongly heterogeneous layer while pointing out similar trade-offs between  
629 the two parameters and non-unique solutions for the more homogeneous layer.  
630 These results suggest the lithospheric mantle beneath all three arrays is much  
631 more homogeneous than the crust above it, where most of the scattering and  
632 attenuation takes place.

633 These results agree with observations from previous studies. Kennett (2015)  
634 studied P-wave reflectivity in the lithosphere and asthenosphere in Australia.  
635 Their results point to strong lithospheric heterogeneity being present beneath sta-  
636 tions in the Proterozoic NAC and they suggest correlation lengths of at most a  
637 few kilometres and  $\sim 2\%$  velocity fluctuations in the crust. For the lithospheric  
638 mantle, they propose much larger correlation lengths (10-20 km) and  $\epsilon < 1\%$ .  
639 Kennett and Furumura (2016) and Kennett et al. (2017) also addressed the pres-  
640 ence and interaction of multi-scale lithospheric heterogeneity in the Australian  
641 continent. In their simulations, they combined large scale heterogeneities with  
642 stochastic media and fine scale structure. Their results indicate a wide range of  
643 heterogeneity spatial scales are present and interact within the lithosphere. Their  
644 models contain four different layers for the fine scale structure, two in the crust  
645 and two in the lithospheric mantle, and different horizontal ( $a_H$ ) and vertical ( $a_V$ )  
646 correlation lengths. Their scattering parameters suggest a mildly heterogeneous  
647 asthenospheric mantle ( $a_H = 10$  km,  $a_V = 10$  km,  $\epsilon = 0.5\%$ ) and an increase in

648 the strength of the heterogeneity in the lithosphere-asthenosphere transition zone  
 649 ( $a_H = 5$  km,  $a_V = 1$  km,  $\epsilon = 1$  %). The crust is generally more heterogeneous in  
 650 these models, with  $a_H = 2.6$  km,  $a_V = 0.4$  km for both crustal layers and RMS  
 651 velocity fluctuations of 0.5% and 1.5% for the upper and lower crust respectively.  
 652 At resolvable scales, these values are consistent with our results from the EFMD  
 653 (Table 5).

### 654 **5.3 Limitations and assumptions**

655 A possible source of error in our inversion is the prescribed thickness of the layers  
 656 in our models. The EFMD is sensitive to changes in the bottom depth of the  
 657 different layers, especially for the shallowest layer, as this affects the diffusion  
 658 out of them. For our model type II, we used a priori information on Moho and  
 659 lithosphere-asthenosphere boundary (LAB) depths. As discussed in Section 4,  
 660 however, there is some uncertainty in reported depths, especially for the LAB.  
 661 Our models consider the lithosphere to extend down to 200 km depth for all three  
 662 arrays, but tests of the EFMD with shallower LABs did not produce major changes  
 663 in our results.

664 Previous studies have shown that the strongest inhomogeneities within our  
 665 planet are found in the lithosphere, even if deeper sections can also be heteroge-  
 666 neous (e.g. Shearer and Earle, 2004; Shearer, 2007; Rost et al., 2015). In this study,  
 667 we focused on the characterization of small-scale lithospheric heterogeneities be-  
 668 neath ASAR, PSAR and WRA, with our models extending down to 200 km depth  
 669 in all cases. We interpreted our results under the assumption that the coda en-  
 670 ergy was generated by lithospheric inhomogeneities, even if we are aware that we  
 671 cannot rule out energy contributions from deeper, weaker scatterers. It is unlikely  
 672 that these structures are the dominant source of coda energy throughout the time

673 window used in our analysis and their effect on our results is likely small.

674 Other limitations of our approach are the assumptions for the determination  
675 of the different quality factors in the EFM and the fact that neither the EFM nor  
676 the EFMD take into account phase conversions and reflections at interfaces other  
677 than the free surface. Equation 15b from Korn (1990), which we use in this study,  
678 is based on the assumption that  $Q_s$  and  $Q_{diff}$  are of the same order of magnitude,  
679 even if that is not necessarily always the case. The intrinsic quality factor ( $Q_i$ )  
680 value used in the EFMD was determined by the EFM, with a limitation to a single  
681 scattering layer and a poorly constrained frequency dependence of  $Q_i$ , since  $\alpha$   
682 could not be fully inverted for in the EFM (Section 2.1). Therefore, all layers in  
683 our EFMD models have the same  $Q_i$  and frequency dependence as obtained in the  
684 EFM. The heterogeneity anisotropy observed by Kennett and Furumura (2016)  
685 and Kennett et al. (2017) could be included in future approaches of Bayesian  
686 inversion for heterogeneity structure but given the range of acceptable models  
687 we find and the trade-offs inherent in inverting for scattering parameters we have  
688 demonstrated, we are unsure if anisotropy in scattering could be well resolved with  
689 these kinds of data.



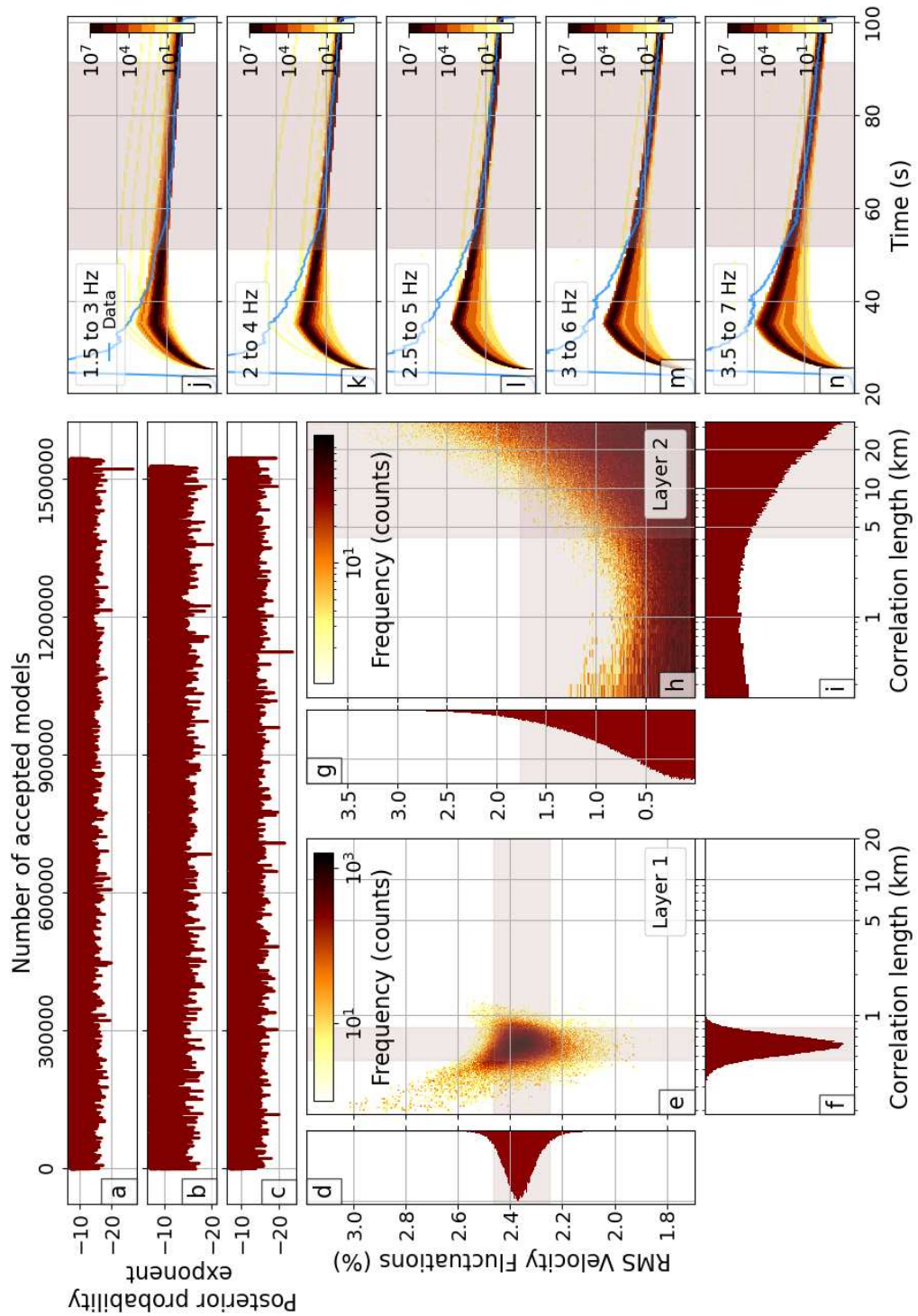


Figure 8: Results from Model type II and PSAR using only the five highest frequency bands from Table 1.

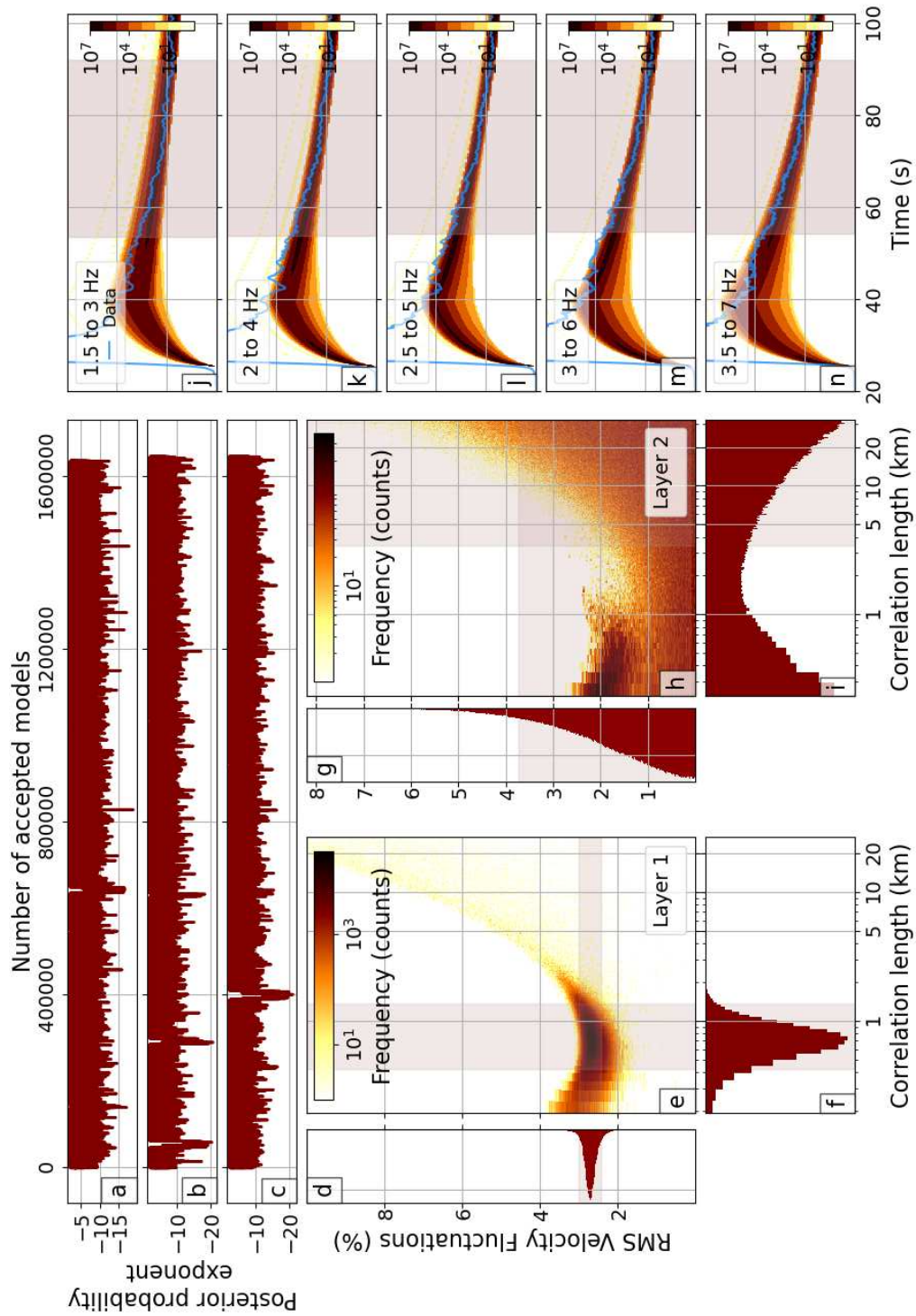


Figure 9: As Fig. 8 but for ASAR.

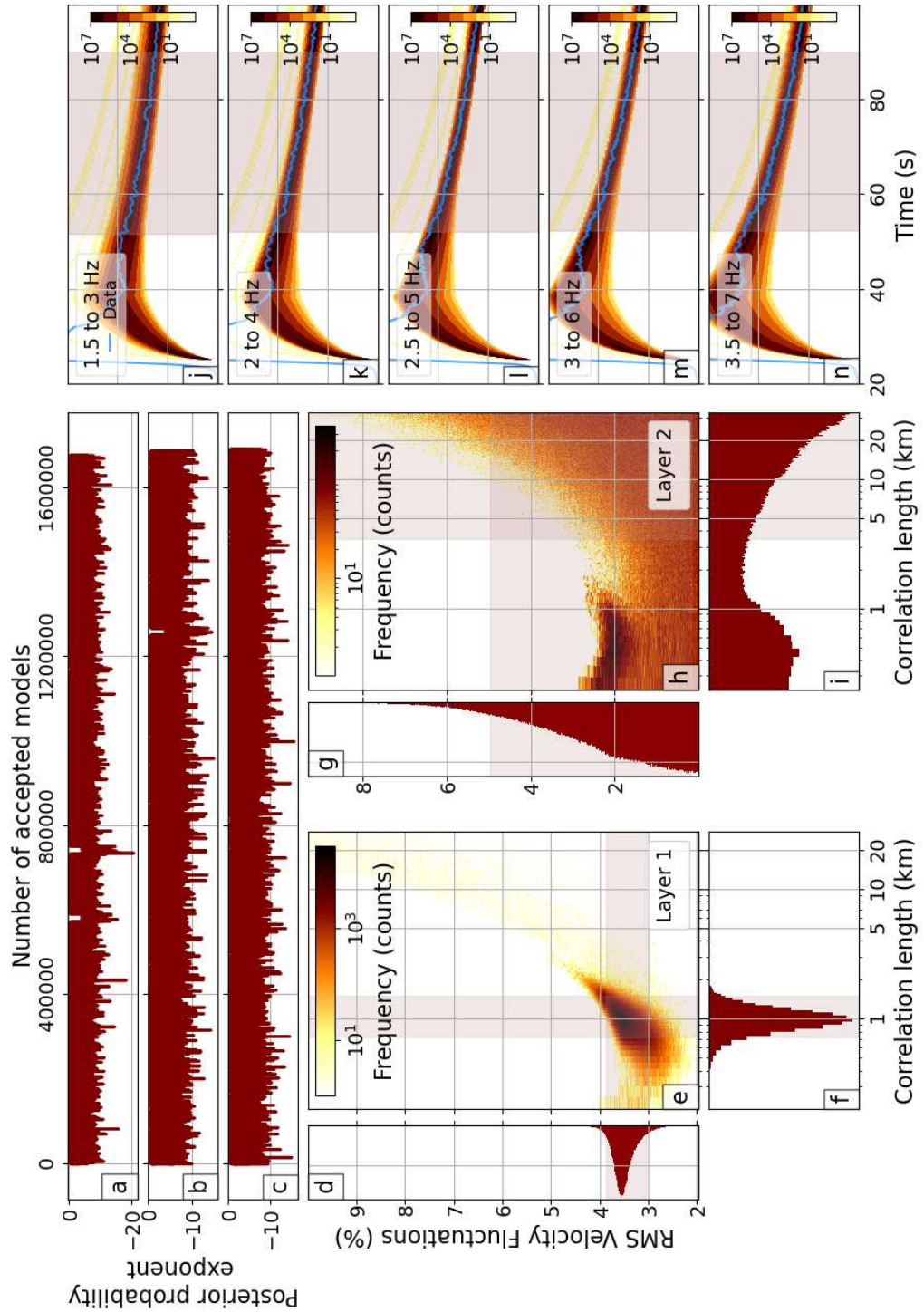


Figure 10: As Fig. 8 but for WRA.

## 6 CONCLUSIONS

For three Australian seismic arrays, we applied the single layer modified Energy Flux Model (EFM) and depth dependent Energy Flux Model (EFMD) to a large dataset which includes events from a wide range of magnitudes, distances and azimuths. This ensures we are thoroughly sampling the structure of the lithosphere beneath the arrays and reduces azimuthal and lateral bias. Our EFM results highlight similarities and differences in the behaviour of the quality factors ( $Q_i$ ,  $Q_{diff}$ ,  $Q_s$ ,  $Q_{comb}$ ) for the three arrays studied here and, therefore, the attenuation structure beneath them. Generally, intrinsic and diffusion quality factors are lower at all frequencies for ASAR than for the other two arrays, which would indicate that attenuation caused by these two mechanisms would be strongest for this array. However, the scattering and total quality factors take similar values for ASAR and WRA, making their heterogeneity and overall attenuation structure comparable and different to PSAR. These results are consistent with the tectonic histories and settings of the areas the arrays are located on. WRA and ASAR lie on the proterozoic North Australian Craton (NAC), but while WRA is situated near its center, ASAR is on its southern border, a margin with more complex and recent tectonic history than the interior of the craton, which correlates with the generally lower quality factor values we observe for ASAR. The EFMD confirms some of these similarities and differences. Our results suggest the crust is more heterogeneous than the lithospheric mantle for all arrays, which could be related to the cratonic nature of the lithosphere in these areas. Correlation lengths in the crust vary from  $\sim 0.2$ – $1.5$  km and RMS velocity fluctuations take values in the 2–4 % range. The scattering structure of the lithospheric mantle, on the other hand, is more complex. Solutions for this layer are not unique, with both low ( $< 2$  km) and high ( $> 5$  km) correlation length values being equally possible. Low

716 velocity fluctuation values are favoured in the inversion results for all arrays, but  
717 the posterior PDFs for ASAR and WRA extend up to  $\sim 6\%$  and  $\sim 7\%$  respectively  
718 and only to  $\sim 3\%$  for PSAR, thus supporting our hypothesis that the similarities  
719 and differences in the heterogeneity structure beneath these arrays are caused by  
720 their different locations on the cratons and the different tectonic histories of these  
721 areas.

722 These results highlight the suitability of Bayesian inversion approaches for the  
723 characterization of lithospheric small-scale structure. Our synthetic tests show  
724 that the combination of the EFMD and our Bayesian inference algorithm can ef-  
725 fectively recover heterogeneity parameters for 1- and 2-layer models. Our approach  
726 provides detailed information about the parameter space and the trade offs and  
727 uncertainties in the determination of the structural parameters. The study of  
728 the posterior PDFs also allows us to determine whether a single set of scattering  
729 parameters can successfully explain our data or whether solutions are not unique.

730 Our study shows that energy flux models can be used for seismic arrays or  
731 groups of stations (PSAR, WRA) and single seismic stations (like the single avail-  
732 able 3-component station at ASAR). The methods rely on teleseismic data, which  
733 makes them suitable for regions with limited local and regional seismicity, such as  
734 our study areas in northern and western Australia. The strength of the hetero-  
735 geneity is not constrained, which makes this technique applicable to strong and  
736 weak scattering regimes and apt to the study of small-scale heterogeneity on Earth  
737 and other planets. Finally, the computational efficiency of the EFMD means it  
738 can be combined with Bayesian inference algorithms to explore wide and complex  
739 parameter spaces. Overall, our study shows that the combination of the EFM and  
740 Bayesian EFMD is an effective tool to quantify heterogeneities in the lithosphere  
741 and can contribute to our understanding of heterogeneity distribution in the Earth.

## 742 **Acknowledgments**

743 This work was supported by the Leeds-York Natural Environment Research Coun-  
744 cil (NERC) Doctoral Training Partnership (DTP) NE/L002574/1, in CASE part-  
745 nership with the Atomic Weapons Establishment (AWE) Blacknest. Andy Nowacki  
746 was supported by NERC (standard grant REMIS: Reliable Earthquake Magnitudes  
747 for Induced Seismicity: NE/R001.154/1).

748 The facilities of IRIS Data Services, and specifically the IRIS Data Manage-  
749 ment Center, were used for access to waveforms, related metadata, and/or derived  
750 products used in this study. IRIS Data Services are funded through the Seismologi-  
751 cal Facilities for the Advancement of Geoscience and EarthScope (SAGE) Proposal  
752 of the National Science Foundation under Cooperative Agreement EAR-1261681.

753 Geoscience Australia operates the Australian National Seismic Network within  
754 Australia, its Territories and across its local region. The network supports the  
755 Joint Australian Tsunami Warning Centre, operated by Geoscience Australia and  
756 the Australian Bureau of Meteorology, which is responsible for issuing tsunami  
757 warning bulletins for Australia and its Territories. The network also contributes  
758 to monitoring earthquakes in the Australian region.

759 Obspy (Krischer et al., 2015) and Matplotlib (Hunter, 2007) were used for data  
760 processing and plotting.

761 The authors would like to thank Vernon Cormier and two anonymous reviewers  
762 for their constructive and helpful comments which contributed to improving the  
763 original manuscript. Discussions with Corinna Roy and Andrew Walker about  
764 Bayesian inference and optimization of Python code are gratefully acknowledged.

765 **References**

- 766 Aitken, A. (2009). The architecture, kinematics, and lithospheric processes of  
767 a compressional intraplate orogen occurring under Gondwana assembly: The  
768 Petermann orogeny, central Australia. *Lithosphere*, 1(6):343–357.
- 769 Aitken, A. R. A., Betts, P. G., Weinberg, R. F., and Gray, D. (2009). Constrained  
770 potential field modeling of the crustal architecture of the Musgrave Province in  
771 central Australia: Evidence for lithospheric strengthening due to crust-mantle  
772 boundary uplift. *Journal of Geophysical Research*, 114(B12):B12405.
- 773 Aki, K. (1969). Analysis of the seismic coda of local earthquakes as scattered  
774 waves. *Journal of Geophysical Research*, 74(2):615–631.
- 775 Aki, K. (1973). Scattering of P waves under the Montana Lasa. *Journal of Geo-*  
776 *physical Research*, 78(8):1334–1346.
- 777 Aki, K. (1980). Attenuation of shear-waves in the lithosphere for frequencies from  
778 0.05 to 25 Hz. *Physics of the Earth and Planetary Interiors*, 21(1):50–60.
- 779 Aki, K. and Chouet, B. (1975). Origin of coda waves: Source, attenuation, and  
780 scattering effects. *Journal of Geophysical Research*, 80(23):3322–3342.
- 781 Alexander, S. S. and Phinney, R. A. (1966). A study of the core-mantle boundary  
782 using P waves diffracted by the Earth’s core. *Journal of Geophysical Research*,  
783 71(24):5943–5958.
- 784 Bayes, T. (1763). LII. An essay towards solving a problem in the doctrine of  
785 chances. By the late Rev. Mr. Bayes, F. R. S. communicated by Mr. Price, in a  
786 letter to John Canton, A. M. F. R. S. *Philosophical Transactions of the Royal*  
787 *Society of London*, 53:370–418.

- 788 Birch, F. (1961). The velocity of compressional waves in rocks to 10 kilobars: 2.  
789 *Journal of Geophysical Research*, 66(7):2199–2224.
- 790 Blake, D. and Kilgour, B. (1998). Geological Regions of Australia  
791 1: 5,000,000 Scale [Dataset]. *Geoscience Australia, Canberra. Available at:*  
792 <http://pid.geoscience.gov.au/dataset/ga/32366>.
- 793 Brooks, S., German, A., Jones, G., and Meng, X.-L., editors (2011). *Handbook of*  
794 *Markov chain Monte Carlo*. CRC Press.
- 795 Cawood, P. and Korsch, R. (2008). Assembling Australia: Proterozoic building of  
796 a continent. *Precambrian Research*, 166(1-4):1–35.
- 797 Chandrasekhar, S. (1950). *Radiative Transfer*. Oxford: Clarendon Press.
- 798 Christensen, N. I. and Mooney, W. D. (1995). Seismic velocity structure and  
799 composition of the continental crust: A global view. *Journal of Geophysical*  
800 *Research: Solid Earth*, 100(B6):9761–9788.
- 801 Clitheroe, G., Gudmundsson, O., and Kennett, B. L. N. (2000). The crustal thick-  
802 ness of Australia. *Journal of Geophysical Research: Solid Earth*, 105(B6):13697–  
803 13713.
- 804 Corbishley, D. J. (1970). Structure under Seismic Arrays. *Geophysical Journal*  
805 *International*, 21(5):415–425.
- 806 Cormier, V. F. (1982). The effect of attenuation on seismic body waves. *Bulletin*  
807 *of the Seismological Society of America*, 72(6B):S169–S200.
- 808 Debayle, E. and Kennett, B. L. N. (2000). The Australian continental upper  
809 mantle: Structure and deformation inferred from surface waves. *Journal of*  
810 *Geophysical Research: Solid Earth*, 105(B11):25423–25450.



- 811 Domínguez, T. and Rebollar, C. J. (1997). Regional variations of seismic attenua-  
 812 tion from coda and Lg waves in northern Baja California. *Journal of Geophysical*  
 813 *Research: Solid Earth*, 102(B7):15259–15268.
- 814 Drummond, B. and Collins, C. (1986). Seismic evidence for underplating of the  
 815 lower continental crust of Australia. *Earth and Planetary Science Letters*, 79(3-  
 816 4):361–372.
- 817 Dziewonski, A. M. and Anderson, D. L. (1981). Preliminary reference Earth model.  
 818 *Physics of the Earth and Planetary Interiors*, 25(4):297–356.
- 819 Emoto, K., Sato, H., and Nishimura, T. (2010). Synthesis of vector wave envelopes  
 820 on the free surface of a random medium for the vertical incidence of a plane  
 821 wavelet based on the Markov approximation. *Journal of Geophysical Research*,  
 822 115(B8):B08306.
- 823 Etgen, J., Gray, S. H., and Zhang, Y. (2009). An overview of depth imaging in  
 824 exploration geophysics. *Geophysics*, 74(6):WCA5–WCA17.
- 825 Fang, Y. and Müller, G. (1996). Attenuation Operators and Complex Wave Veloci-  
 826 ties for Scattering in Random Media. *Pure and Applied Geophysics*, 148(1):269–  
 827 285.
- 828 Fehler, M., Hoshihara, M., Sato, H., and Obara, K. (1992). Separation of scat-  
 829 tering and intrinsic attenuation for the Kanto-Tokai region, Japan, using mea-  
 830 surements of S -wave energy versus hypocentral distance. *Geophysical Journal*  
 831 *International*, 108(3):787–800.
- 832 Fichtner, A., Kennett, B. L., Igel, H., and Bunge, H. P. (2009). Full seismic  
 833 waveform tomography for upper-mantle structure in the Australasian region  
 834 using adjoint methods. *Geophysical Journal International*, 179(3):1703–1725.

- 835 Fielitz, D. and Wegler, U. (2015). Intrinsic and scattering attenuation as derived  
836 from fluid induced microseismicity at the German Continental Deep Drilling  
837 site. *Geophysical Journal International*, 201(3):1346–1361.
- 838 Flatté, S. M. and Wu, R.-S. (1988). Small-scale structure in the lithosphere and as-  
839 thenosphere deduced from arrival time and amplitude fluctuations at NORSAR.  
840 *Journal of Geophysical Research*, 93(B6):6601.
- 841 Ford, H. A., Fischer, K. M., Abt, D. L., Rychert, C. A., and Elkins-Tanton, L. T.  
842 (2010). The lithosphere–asthenosphere boundary and cratonic lithospheric lay-  
843 ering beneath Australia from Sp wave imaging. *Earth and Planetary Science*  
844 *Letters*, 300(3-4):299–310.
- 845 Frankel, A. and Wennerberg, L. (1987). Energy-Flux Model of Seismic Coda:  
846 Separation of Scattering and Intrinsic Attenuation. *Bulletin of the Seismological*  
847 *Society of America*, 77(4):1223–1251.
- 848 Gaebler, P. J., Eulenfeld, T., and Wegler, U. (2015a). Seismic scattering and ab-  
849 sorption parameters in the W-Bohemia/Vogtland region from elastic and acous-  
850 tic radiative transfer theory. *Geophysical Journal International*, 203(3):1471–  
851 1481.
- 852 Gaebler, P. J., Sens-Schönfelder, C., and Korn, M. (2015b). The influence of crustal  
853 scattering on translational and rotational motions in regional and teleseismic  
854 coda waves. *Geophysical Journal International*, 201(1):355–371.
- 855 Goleby, B. R., Shaw, R. D., Wright, C., Kennett, B. L. N., and Lambeck, K.  
856 (1989). Geophysical evidence for 'thick-skinned' crustal deformation in central  
857 Australia. *Nature*, 337(6205):325–330.

- 858 Gusev, A. and Abubakirov, I. (1987). Monte-Carlo simulation of record envelope of  
859 a near earthquake. *Physics of the earth and planetary interiors*, 49(1-2):30–36.
- 860 Hastings, W. K. (1970). Monte Carlo sampling methods using Markov chains and  
861 their applications. *Biometrika*, 57(1):97–109.
- 862 Helmberger, D. V. (1968). The crust-mantle transition in the Bering sea. *Bulletin*  
863 *of the Seismological Society of America*, 58(1):179–214.
- 864 Hirose, T., Nakahara, H., and Nishimura, T. (2019). A Passive Estimation Method  
865 of Scattering and Intrinsic Absorption Parameters From Envelopes of Seis-  
866 mic Ambient Noise Cross-Correlation Functions. *Geophysical Research Letters*,  
867 46(7):3634–3642.
- 868 Hock, S. and Korn, M. (2000). Random heterogeneity of the lithosphere across the  
869 Trans-European Suture Zone. *Geophysical Journal International*, 141(1):57–70.
- 870 Hock, S., Korn, M., Ritter, J. R. R., and Rothert, E. (2004). Mapping random  
871 lithospheric heterogeneities in northern and central Europe. *Geophysical Journal*  
872 *International*, 157(1):251–264.
- 873 Hunter, J. D. (2007). Matplotlib: A 2D Graphics Environment. *Computing in*  
874 *Science & Engineering*, 9(3):90–95.
- 875 Kennett, B. (2015). Lithosphere–asthenosphere P-wave reflectivity across Aus-  
876 tralia. *Earth and Planetary Science Letters*, 431:225–235.
- 877 Kennett, B. and Saygin, E. (2015). The nature of the Moho in Australia from  
878 reflection profiling: A review. *GeoResJ*, 5:74–91.
- 879 Kennett, B. and Sippl, C. (2018). Lithospheric discontinuities in Central Australia.  
880 *Tectonophysics*, 744(June):10–22.

- 881 Kennett, B. L., Fichtner, A., Fishwick, S., and Yoshizawa, K. (2013). Australian  
882 seismological reference model (AuSREM): mantle component. *Geophysical Jour-*  
883 *nal International*, 192(2):871–887.
- 884 Kennett, B. L., Yoshizawa, K., and Furumura, T. (2017). Interactions of multi-  
885 scale heterogeneity in the lithosphere: Australia. *Tectonophysics*, 717:193–213.
- 886 Kennett, B. L. N. and Engdahl, E. R. (1991). Traveltimes for global earthquake lo-  
887 cation and phase identification. *Geophysical Journal International*, 105(2):429–  
888 465.
- 889 Kennett, B. L. N. and Furumura, T. (2016). Multiscale seismic heterogeneity in the  
890 continental lithosphere. *Geochemistry, Geophysics, Geosystems*, 17(3):791–809.
- 891 Kennett, B. L. N. and Salmon, M. (2012). AuSREM: Australian Seismological  
892 Reference Model. *Australian Journal of Earth Sciences*, 59(8):1091–1103.
- 893 Kennett, B. L. N., Salmon, M., Saygin, E., and Group, A. W. (2011). AusMoho:  
894 the variation of Moho depth in Australia. *Geophysical Journal International*,  
895 187(2):946–958.
- 896 Korn, M. (1990). A modified energy flux model for lithospheric scattering of  
897 teleseismic body waves. *Geophysical Journal International*, 102(1):165–175.
- 898 Korn, M. (1993). Determination of Site-Dependent Scattering Q From P -Wave  
899 Coda Analysis With an Energy-Flux Model. *Geophysical Journal International*,  
900 113(1):54–72.
- 901 Korn, M. (1997). Modelling the teleseismic P coda envelope: depth dependent  
902 scattering and deterministic structure. *Physics of the Earth and Planetary In-*  
903 *teriors*, 104(1-3):23–36.

- 904 Korsch, R., Goleby, B., Leven, J., and Drummond, B. (1998). Crustal architecture  
905 of central Australia based on deep seismic reflection profiling. *Tectonophysics*,  
906 288(1-4):57–69.
- 907 Krischer, L., Megies, T., Barsch, R., Beyreuther, M., Lecocq, T., Caudron, C.,  
908 and Wassermann, J. (2015). ObsPy: a bridge for seismology into the scientific  
909 Python ecosystem. *Computational Science & Discovery*, 8(1):014003.
- 910 Langston, C. A. (1989). Scattering of teleseismic body waves under Pasadena,  
911 California. *Journal of Geophysical Research*, 94(B2):1935.
- 912 Mahalanobis, P. C. (1936). On the generalized distance in statistics. National  
913 Institute of Science of India.
- 914 Margerin, L. (2005). Introduction To Radiative Transfer Theory. *Geophysical*  
915 *Monograph-American Geophysical Union*, 157:1–47.
- 916 Margerin, L., Bajasas, A., and Campillo, M. (2019). A scalar radiative transfer  
917 model including the coupling between surface and body waves. *Geophysical*  
918 *Journal International*, 219(2):1092–1108.
- 919 Margerin, L., Campillo, M., and Tiggelen, B. (1998). Radiative transfer and diffu-  
920 sion of waves in a layered medium: new insight into coda Q. *Geophysical journal*  
921 *international*, 134(2):596–612.
- 922 Margerin, L. and Nolet, G. (2003). Multiple scattering of high-frequency seismic  
923 waves in the deep Earth: PKP precursor analysis and inversion for mantle  
924 granularity. *Journal of Geophysical Research: Solid Earth*, 108(B11).
- 925 Metropolis, N., Rosenbluth, A. W., Rosenbluth, M. N., Teller, A. H., and Teller,

- 926 E. (1953). Equation of State Calculations by Fast Computing Machines. *The*  
927 *Journal of Chemical Physics*, 21(6):1087–1092.
- 928 Metropolis, N. and Ulam, S. (1949). The Monte Carlo Method. *Journal of the*  
929 *American Statistical Association*, 44(247):335–341.
- 930 Myers, J. S. (1990). Precambrian tectonic evolution of part of Gondwana, south-  
931 western Australia. *Geology*, 18(6):537.
- 932 Nakahara, H. and Yoshimoto, K. (2011). Radiative transfer of elastic waves in two-  
933 dimensional isotropic scattering media: Semi-analytical approach for isotropic  
934 source radiation. *Earth, Planets and Space*, 63(6):459–468.
- 935 Przybilla, J. and Korn, M. (2008). Monte Carlo simulation of radiative energy  
936 transfer in continuous elastic random media-three-component envelopes and nu-  
937 merical validation. *Geophysical Journal International*, 173(2):566–576.
- 938 Randall, G. E. (1994). Efficient calculation of complete differential seismograms  
939 for laterally homogeneous earth models. *Geophysical Journal International*,  
940 118(1):245–254.
- 941 Rautian, T. G. and Khalturin, V. I. (1978). The use of the coda for determination  
942 of the earthquake source spectrum. *Bulletin of the Seismological Society of*  
943 *America*, 68(4):923–948.
- 944 Raymond, O., Totterdell, J., Stewart, A., and Woods, M. (2018). Australian  
945 Geological Provinces, 2018. *Geoscience Australia, Canberra. Available at:*  
946 *<http://pid.geoscience.gov.au/dataset/ga/116823>*.
- 947 Ritter, J. R. R., Shapiro, S. A., and Schechinger, B. (1998). Scattering parameters

- 948 of the lithosphere below the Massif Central, France, from teleseismic wavefield  
949 records. *Geophysical Journal International*, 134(1):187–198.
- 950 Rost, S., Earle, P. S., Shearer, P. M., Frost, D. A., and Selby, N. D. (2015). Chapter  
951 12: Seismic detections of small-scale heterogeneities in the Deep Earth. *The*  
952 *Earth’s Heterogeneous Mantle: A Geophysical, Geodynamical, and Geochemical*  
953 *Perspective*, pages 1–530.
- 954 Salmon, M., Kennett, B., Stern, T., and Aitken, A. (2013a). The Moho in Australia  
955 and New Zealand. *Tectonophysics*, 609:288–298.
- 956 Salmon, M., Kennett, B. L. N., and Saygin, E. (2013b). Australian Seismological  
957 Reference Model (AuSREM): crustal component. *Geophysical Journal Interna-*  
958 *tional*, 192(1):190–206.
- 959 Sanborn, C. J., Cormier, V. F., and Fitzpatrick, M. (2017). Combined effects of  
960 deterministic and statistical structure on high-frequency regional seismograms.  
961 *Geophysical Journal International*, 210(2):1143–1159.
- 962 Sato, H. (1977). Energy propagation including scattering effects single isotropic  
963 scattering approximation. *Journal of Physics of the Earth*, 25(1):27–41.
- 964 Sato, H. (1984). Attenuation and envelope formation of three-component seis-  
965 mograms of small local earthquakes in randomly inhomogeneous lithosphere.  
966 *Journal of Geophysical Research: Solid Earth*, 89(B2):1221–1241.
- 967 Sato, H. (2006). Synthesis of vector wave envelopes in three-dimensional random  
968 elastic media characterized by a Gaussian autocorrelation function based on  
969 the Markov approximation: Plane wave case. *Journal of Geophysical Research:*  
970 *Solid Earth*, 111(B6):n/a–n/a.

- 971 Sato, H. (2007). Synthesis of vector wave envelopes in three-dimensional random  
972 elastic media characterized by a Gaussian autocorrelation function based on the  
973 Markov approximation: Spherical wave case. *Journal of Geophysical Research*,  
974 112(B1):B01301.
- 975 Sato, H. and Emoto, K. (2017). Synthesis of a scalar wavelet intensity propagat-  
976 ing through von Kármán-type random media: joint use of the radiative transfer  
977 equation with the Born approximation and the Markov approximation. *Geo-  
978 physical Journal International*, 211(1):512–527.
- 979 Sato, H. and Emoto, K. (2018). Synthesis of a Scalar Wavelet Intensity Propagating  
980 Through von Kármán-type Random Media: Radiative Transfer Theory Using  
981 the Born and Phase-Screen Approximations. *Geophysical Journal International*,  
982 pages 909–923.
- 983 Sato, H., Fehler, M. C., and Maeda, T. (2012). *Seismic Wave Propagation and  
984 Scattering in the Heterogeneous Earth : Second Edition*. Springer Berlin Hei-  
985 delberg, Berlin, Heidelberg.
- 986 Shapiro, S. A. and Kneib, G. (1993). Seismic Attenuation By Scattering: Theory  
987 and Numerical Results. *Geophysical Journal International*, 114(2):373–391.
- 988 Shearer, P. M. (2007). Seismic scattering in the deep earth. *Treatise on geophysics*,  
989 1:695–730.
- 990 Shearer, P. M. and Earle, P. S. (2004). The global short-period wavefield modelled  
991 with a Monte Carlo seismic phonon method. *Geophysical Journal International*,  
992 158(3):1103–1117.
- 993 Simons, F. J., Zielhuis, A., and der Hilst, R. D. (1999). The deep structure of the  
994 Australian continent inferred from surface wave tomography. *Lithos*, 48:17–43.



- 995 Sipkin, S. A. and Revenaugh, J. (1994). Regional variation of attenuation and  
996 travel time in china from analysis of multiple-scs phases. *Journal of Geophysical*  
997 *Research: Solid Earth*, 99(B2):2687–2699.
- 998 Sippl, C. (2016). Moho geometry along a north-south passive seismic transect  
999 through Central Australia. *Tectonophysics*, 676:56–69.
- 1000 Snieder, R. (2006). The Theory of Coda Wave Interferometry. *Pure and Applied*  
1001 *Geophysics*, 163(2-3):455–473.
- 1002 Tarantola, A. (2005). *Inverse problem theory and methods for model parameter*  
1003 *estimation*, volume 89. Siam.
- 1004 Thorbecke, J., Slob, E., Brackenhoff, J., van der Neut, J., and Wapenaar, K.  
1005 (2017). Implementation of the Marchenko method. *Geophysics*, 82(6):WB29–  
1006 WB45.
- 1007 van der Neut, J., Wapenaar, K., Thorbecke, J., Slob, E., and Vasconcelos, I.  
1008 (2015). An illustration of adaptive Marchenko imaging. *The Leading Edge*,  
1009 34(7):818–822.
- 1010 Wellman, P. (1998). Mapping of geophysical domains in the Australian continental  
1011 crust using gravity and magnetic anomalies. In *Structure and evolution of the*  
1012 *Australian continent*, pages 59–71. American Geophysical Union, Washington,  
1013 D.C: AGU.
- 1014 Wu, R.-S. (1985). Multiple scattering and energy transfer of seismic waves – sepa-  
1015 ration of scattering effect from intrinsic attenuation – I. Theoretical modelling.  
1016 *Geophysical Journal International*, 82(1):57–80.

- 1017 Wu, R.-S. and Aki, K. (1988). Introduction: Seismic Wave Scattering in Three-  
1018 dimensionally Heterogeneous Earth. In *Scattering and Attenuations of Seismic*  
1019 *Waves, Part I*, pages 1–6. Birkhäuser Basel, Basel.
- 1020 Yoshizawa, K. and Kennett, B. L. N. (2015). The lithosphere-asthenosphere tran-  
1021 sition and radial anisotropy beneath the Australian continent. *Geophysical Re-*  
1022 *search Letters*.
- 1023 Zelt, C. A. and Barton, P. J. (1998). Three-dimensional seismic refraction tomog-  
1024 raphy: A comparison of two methods applied to data from the Faeroe Basin.  
1025 *Journal of Geophysical Research: Solid Earth*, 103(B4):7187–7210.